https://doi.org/10.5194/egusphere-2026-1840
Preprint. Discussion started: 23 April 2026

Turbulence and mixing along a microtidal and stratified estuary-shelf transition

Débora Barros[1], Lauren Ross[2], Carlos A.F. Schettini[1]

[1]Institute of Oceanography, Federal University of Rio Grande, Rio Grande, 90000, Brazil
[2] Department of Civil and Environmental Engineering, University of Maine, Orono, postal code, USA

Correspondence to: Carlos A.F. Schettini (guto.schettini@gmail.com)

Abstract. This study investigates the hydrodynamic and mixing processes at the estuary–shelf transition of a microtidal system, and the buoyant plume generated at the Patos Lagoon mouth (Brazil). Using measurements of turbulent kinetic energy (TKE) dissipation (ϵ), current velocities, salinity, and temperature collected during a high-discharge period (~9,400 $m^3 s^{-1}$), we characterize the spatial evolution of turbulence and mixing along the channel, from the source to the buoyancy-driven plume region. Observations show that the jetty-constrained inlet acts as a morphological nozzle, forcing the flow to remain supercritical (*Fri* > 1) for several kilometres onto the inner shelf. Despite strong stratification, intense shear-driven turbulence was observed, with TKE dissipation rates (ϵ) reaching 10^{-3} W kg^{-1} near the mouth, comparable to values reported in high-energy mesotidal and macrotidal systems. Analysis of the buoyancy Reynolds number (*Reb*) and the gradient Richardson number (*Ri*) indicates that inertial forcing overcomes buoyancy suppression, maintaining a predominantly turbulent regime (*Reb* > 200) at the plume front. These results demonstrate that, in narrow, high-discharge estuarine outlets, morphological confinement and sustained supercritical flow govern the near-field evolution of buoyant plumes, maintaining vigorous mixing even under pronounced density stratification.

1 Introduction

Buoyant plumes are critical hydrodynamic structures in coastal environments, as they represent the primary interaction in the flow transition between laterally constrained estuaries and the adjacent shelf (Fennel and Mutzke, 1997). Plumes are responsible for the injection of freshwater and momentum into the inner shelf, transporting suspended sediments, organic matter, nutrients, and pollutants (Horner-Devine et al., 2015). These inputs play a key role in regulating the coastal carbon budget by stimulating biological production and respiration on the inner shelf (Schettini et al., 1998; Cai et al., 2013; Lohrenz et al., 2013), thereby highlighting the importance of physical mixing in modulating these processes (Sims et al., 2022; Wu et al., 2023).

The dynamics of plumes are driven primarily by the density gradient between the low-salinity freshwater discharge and the denser coastal waters, as well as the momentum associated with the estuarine outflow (Horner-Devine et al., 2015; McPherson

https://doi.org/10.5194/egusphere-2026-1840
Preprint. Discussion started: 23 April 2026

et al., 2019). These mechanisms control the plume's basic structure, including its lateral spreading, vertical layering, and the efficiency of mixing with the surrounding ocean.

From a structural perspective, plume dynamics have classically been described in terms of two regions: the near-field (or inner-field) and the far-field (or outer-field) (Jirka et al., 1981). Within the near-field, the low-density discharge maintains high velocities and is heavily influenced by momentum, characterizing it as a buoyant jet. In this region, momentum dominates over buoyancy, driving high levels of turbulence and intense mixing with the adjacent coastal waters. During the initial stage of plume evolution, the vertical structure is highly stratified, featuring a relatively thin, low-density surface layer flowing energetically over a higher-density ambient water mass.

As the plume moves away from the near-field region, a regime shift occurs in which the initial jet momentum is progressively dissipated, allowing buoyancy to exert greater control over the flow. According to Hetland (2005), this transition between the near-field and the far-field happens when inertial forces cease to dominate the system in favour of gravitational forces. This point is defined by the Froude number decreasing below unity, marking the shift from a supercritical to a subcritical regime and representing a structural change in the balance of forces governing the plume.

The regime transition zone is particularly relevant regarding mixing processes, as it may be linked to the occurrence of internal hydraulic jumps. These features represent areas of intense energy dissipation, playing a crucial role in momentum redistribution and driving vertical mixing between layers. Internal hydraulic jumps can account for up to one-third of the total momentum dissipation in the interfacial layer of stratified estuarine systems (McPherson et al., 2020). Despite their importance, the morphology, structure, and spatial variability of these mechanisms remain poorly understood in complex natural environments (Thorpe et al., 2017).

Horner-Devine et al. (2015) propose a more detailed approach to the evolution of buoyant plumes, expanding the classical two-region regime of Jirka et al. (1981). This classification defines four distinct regions: (i) the source region, strongly controlled by the mouth geometry and estuarine conditions; (ii) the buoyancy-forced plume region, where barotropic and baroclinic pressure gradients, along with turbulence and mixing, govern the flow; (iii) the mid-field region, characterized by a diminishing influence of initial momentum and the increasing importance of Earth's rotation, friction, wind, and bathymetric interaction; and (iv) the far-field, associated with larger spatial scales, quasi-geostrophic dynamics, and alongshore transport.

Mixing plays a central role in the plume's spatial and temporal evolution, eroding vertical gradients and dissipating kinetic energy. This mixing occurs primarily through instabilities at the fluid interface, as well as through frontal processes and wind forcing (Ivey et al., 2008; Stacey et al., 2012; Spicer et al., 2022). However, direct turbulence measurements within the plume itself are notoriously difficult to perform, despite being fundamental for identifying and understanding the physical

https://doi.org/10.5194/egusphere-2026-1840
Preprint. Discussion started: 23 April 2026

mechanisms responsible for mixing (Geyer et al., 2010). Observational studies of buoyant plumes remain scarce at both temporal and spatial scales, limiting a detailed description of plume water transport and mixing processes, especially in the frontal region (Cole et al., 2020; Delatolas et al., 2023). In addition, most existing studies of plume dynamics and turbulence are concentrated in mesotidal and macrotidal estuaries (MacDonald and Geyer, 2004; MacDonald et al., 2007; Wang et al., 2020; Spicer et al., 2022), whereas comparatively few have focused on microtidal systems (Alvarez-Silva et al., 2026). This highlights an important gap, as microtidal environments provide a valuable framework to isolate and investigate non-tidal forcings and their role in controlling plume structure and mixing dynamics. Furthermore, there is a lack of comparative studies integrating turbulence measurements across different estuarine systems, which could reveal fundamental relationships between plume parameters and the transverse distribution and magnitude of TKE dissipation (ϵ) (Delatolas et al., 2023).

Given the aforementioned gaps, this study aims to investigate the source and buoyancy-forced plume regions through in-situ observations, assessing how mouth morphology modulates the hydrodynamic regime, turbulence, and mixing at the estuary-shelf transition zone. To this end, the following research questions are addressed: (1) How does channel morphology affect the along-channel density and velocity fields of a buoyant river plume from a microtidal estuarine system? (2) How does the interplay between buoyancy suppression and shear production vary along the plume? (3) How does this balance influence the spatial evolution of turbulent kinetic energy dissipation (ϵ) across the transition from the estuarine channel into the plume?

This paper is organized as follows: Section 2 describes the study area and its primary characteristics; Section 3 outlines the methods; Sections 4 and 5 discuss the results and their physical implications; and finally, Section 6 concludes the study by proposing a conceptual interpretation of the plume's energetic state and the morphological controls governing the estuary-shelf transition.

2. Study Area

The study area comprises the Rio Grande Channel, at the mouth of the Patos Lagoon, and the adjacent coastal region in Southern Brazil (32° S / 52° W; Fig. 1). The Patos Lagoon is the world's largest choked coastal lagoon, with an area of approximately 10,000 km², roughly 250 km in length, up to 40 km in width, and an average depth of 5 m (Kjerfve & Magill, 1989; Miranda et al., 2002). At its southern end, the system discharges into the South Atlantic Ocean through the Rio Grande Channel. This region constitutes a critical estuarine-to-shelf transition zone, hereafter referred to as the Patos Lagoon inlet for the purpose of geophysical comparison with other outflow systems.

Flow discharge is forced through a narrow 500 m wide channel, approximately 20 m deep, marking the narrowest cross-section of the system (Fig. 1b, c). The inlet is fixed by jetties extending roughly 4 km offshore. These structures constrain the flow, accelerating currents and directly shaping the spatial distribution of the effluent jet. Previous geomorphological and

https://doi.org/10.5194/egusphere-2026-1840
Preprint. Discussion started: 23 April 2026

hydrodynamic research suggests that mouth morphology and bathymetric variability are key factors in structuring the flow and the system's hydrodynamic response (Kirinus et al., 2012). As a result, the discharge is predominantly ebb-directed, carrying low-salinity waters and generating a buoyant plume on the adjacent shelf (Möller et al., 2001; Cruz & Schettini, 2025).

The local astronomical tide is microtidal and mixed, with a diurnal dominance, featuring a mean range of 0.4 m (Möller et al., 2007). The influence of the astronomical tide on local circulation is minor compared to the effects of atmospheric forcing and river discharge. Water level variability and circulation in the region are dominated by meteorological components associated with synoptic systems (cold fronts), which control the inflow and outflow of water through the mouth (Santa-Rosa and Schettini, 2024; Barros et al., 2025; Miranda et al., 2026).

The system's mean river discharge is on the order of 2,400 $m^3 s^{-1}$ (Vaz et al., 2006), exhibiting strong interannual variability, with values reaching approximately 12,000 $m^3 s^{-1}$ during intense flood periods (Hartmann and Schettini, 1991; Marques et al., 2014), reflecting the system's capacity to export large volumes of freshwater and suspended material to the adjacent shelf (Simão et al., 2026). Most of the fluvial input occurs through the Guaíba system at the northern end of the lagoon (Fig. 1a). Notably, there is no direct relationship between river discharge and the water flux through the mouth, as the latter is primarily determined by wind conditions (Santa-Rosa and Schettini, 2024).

Local winds affect water level variability within the lagoon, while remote winds dominate the circulation in the estuary–shelf transition zone (Hartmann and Schettini, 1991; Möller et al., 1996; Möller et al., 2001; Fernandes et al., 2005). Predominant north-easterly winds induce an oceanward barotropic pressure gradient, intensifying freshwater discharge and favouring plume expansion onto the continental shelf. In contrast, south-westerly winds promote coastal sea-level rise through Ekman transport, establishing a landward pressure gradient and favouring flood conditions within the estuary. During high river discharge episodes (exceeding approximately 4,000 $m^3 s^{-1}$), however, the south-west wind effect is overcome by the fluvial forcing, resulting in a persistent ebb regime (Möller et al., 2001; Monteiro et al., 2011). Prevailing winds in the region are aligned along the N–NE and S–SW quadrants, roughly parallel to the main axis of the Patos Lagoon, which promotes efficient hydrodynamic responses throughout the lagoon system (Möller and Castaing, 1999). This geometric configuration contributes to the strong modulation of estuarine circulation and the coastal plume by synoptic events, affecting plume orientation, extent, and persistence, as well as its interaction with shelf circulation (Ávila and Calil, 2018).

Previous studies on the Patos Lagoon plume have been predominantly based on numerical modelling. Initial research investigated the structure and seasonal variability of the regional plume using hydrodynamic models with relatively limited spatial and temporal resolution (Piola et al., 2005; Soares et al., 2007a,b). Subsequent investigations furthered the understanding of the physical mechanisms controlling plume formation and behaviour, highlighting the roles of wind forcing, stratification, and three-dimensional circulation (Marques et al., 2009; Monteiro et al., 2011). Additionally, studies have

https://doi.org/10.5194/egusphere-2026-1840
Preprint. Discussion started: 23 April 2026

addressed the importance of straining and advection processes in modulating stratification within the Patos Lagoon coastal plume (Marques et al., 2010).

Burrage et al. (2008) and Zavialov et al. (2018) explored the interaction between the Patos Lagoon plume and the Rio de la Plata buoyancy currents using remote sensing. While these studies enhanced the understanding of surface dynamics, direct in-situ measurements of the plume's sub-surface structure remain lacking, especially in the near-field zone. Although the internal dynamics within the Rio Grande Channel were recently detailed by Barros et al. (2025), describing the inlet as a highly energetic and stratified environment, the region immediately seaward of the mouth (Fig. 1) remains poorly sampled. In this area, the interplay between synoptic forcing, high river discharge, and complex bathymetry drives intense hydrodynamic variability. Consequently, this region is particularly relevant for investigating mixing processes, energy dissipation, and plume dynamics at the estuary–shelf interface.

https://doi.org/10.5194/egusphere-2026-1840
Preprint. Discussion started: 23 April 2026

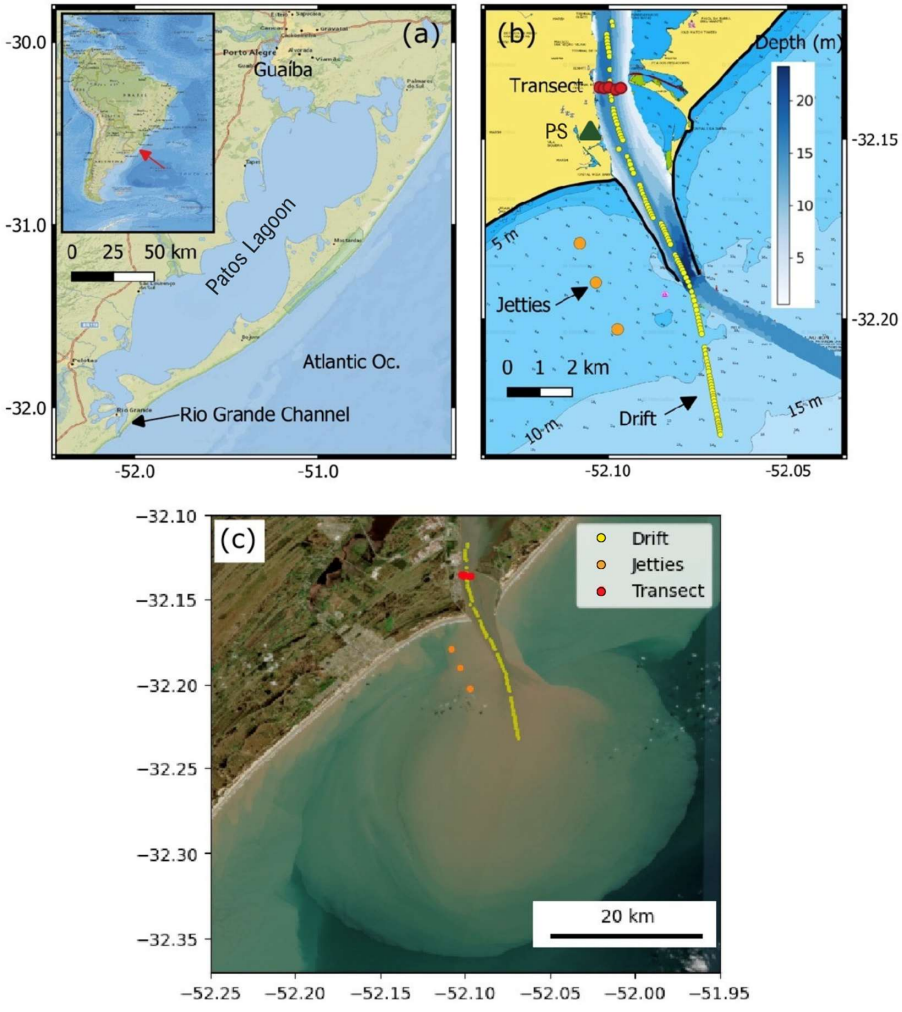

145

Figure 1: Study area location and sampling design. **(a)** Regional setting showing the Patos Lagoon choked system and its connection to the South Atlantic Ocean via the Rio Grande Channel. **(b)** Detailed view of the estuarine–shelf transition; yellow dots represent the Lagrangian track (Drift), orange dots indicate the baseline stations near the breakwaters (Jetties), and red dots show the cross-channel section (Transect). The green triangle (PS) indicates the Rio Grande Pilot Station, the source for meteorological and water level data. Bathymetric contours and
150 the nautical chart emphasize the jetty-constrained morphology. **(c)** Sampling stations overlaid on a Sentinel-2 true-colour image acquired on 18 July 2022, displaying the turbid surface plume during the survey period. This figure was created using QGIS. Panel (a) is based on the XYZ tiles from Esri National Geographic. Panel (b) is based on Brazilian Navy nautical chart No. 2110, available as a GeoTIFF at: https://www.marinha.mil.br/chm/dados-do-segnav/cartas-raster.

https://doi.org/10.5194/egusphere-2026-1840
Preprint. Discussion started: 23 April 2026

3. Materials and Methods

3.1 Fieldwork Design and Data Collection

The fieldwork was designed to capture the spatial variability of the vertical structure of current velocities, water properties, and mixing along the thalweg over the transition from the lagoon inlet and channel to the adjacent shelf, and into the buoyant plume beyond the jetties. The survey was conducted on 18 July 2022, coinciding with a Sentinel satellite overpass with clear-sky conditions, enabling a spatial match between in-situ data and the surface extent of the plume (Fig. 1c). During the field survey, outflow currents predominated, consistent with the conditions described in Section 2, where inflow and outflow at the mouth are primarily modulated by a subtidal wind-driven regime, with astronomical tides playing a minor role.

Considering the limited influence of astronomical tides in the region, the sampling strategy prioritized spatial coverage over tidal phase, and the field campaign was organized into three segments: thalweg drift (Drift), inner shelf outside the jetties (Jetties), and cross-sectional transect (Transect), as referred to hereafter (Fig 1). The Drift segment collected over ~2h and 20min (11:21-13:40 LT) represents the main dataset of the experiment, aiming to capture the longitudinal transition from channelized flow to the early buoyant plume evolution. This segment involved a Lagrangian drift along the thalweg of the channel (with the boat moving passively with the outflow), represented by yellow dots in Figure 1b and 1c, totalling 108 microstructure profiles collected over approximately 13 km. While small adjustments were required inside the channel to compensate for wind-induced drag and maintain the boat within the thalweg, no corrections to the track were made once outside the inlet. The microstructure profiles were collected with a Rockland Scientific MicroCTD, which will be elaborated upon later in this section.

Subsequently, two complementary sampling segments were performed to characterize the boundary conditions. The Jetties segment (14:30-14:50 LT) was conducted on the inner shelf adjacent to the jetties (orange dots, Fig. 1b and 1c) to provide baseline values of TKE dissipation outside the buoyant plume, comprising 17 microstructure profiles across three stations. Finally, the Transect segment (15:45-16:30 LT) consisted of a cross-channel section at the upstream portion of the study area (red dots, Fig. 1b and 1c). This segment included 26 profiles distributed across five stations (~ 5 profiles per station), designed to capture cross-channel hydrographic variability and quantify the volume outflow discharge during the survey.

During the Drift, Transect and Jetties sampling, current velocities were recorded concurrently using a vessel-mounted Teledyne RDI Workhorse 1200 kHz Acoustic Doppler Current Profiler (ADCP) operating in bottom-tracking mode. The instrument was configured with a ping interval of 0.5 s and a vertical bin size of 0.25 m, with the first measurement bin located approximately 1.5 m below the water surface. Horizontal positioning was determined via a GPS unit directly connected to the ADCP system, with an estimated positional uncertainty of ~5 m. The ADCP operated continuously throughout the field campaign, providing

https://doi.org/10.5194/egusphere-2026-1840
Preprint. Discussion started: 23 April 2026

uninterrupted velocity measurements along the survey track. The total water flow across the transect segment was obtained from direct measurements using an ADCP, processed with the WinRiver II software provided by Teledyne RDI.

Salinity and temperature vertical profiles were recorded with a Rinko Profiler CTD (by JFE Advantech LTD) and with a Conductivity-Temperature Sensor (JAC CT) integrated into a Rockland Scientific microstructure profiler (MicroCTD). The MicroCTD recorded shear by two orthogonally mounted shear probes operating at a sampling rate of 512 Hz. The shear profiles were used to estimate turbulence in terms of TKE dissipation rate (ϵ).

The MicroCTD was deployed a total of 152 times in the downward profiling mode at the locations indicated in Figure 1b and 1c, and lowered vertically using a weighted collar to ensure a controlled descent speed of approximately 0.8 m s^{-1} and an angle of attack below 5° (Lueck, 2013; Lueck et al., 2013; Ross et al., 2019, Barros et al., 2025). The MicroCTD data were georeferenced and synchronized with the ADCP data. For each MicroCTD cast, there is a corresponding vertical profile of horizontal velocities, *u* and *v*, time-averaged over a one-minute interval.

Additional environmental data, including wind, water level, and Eulerian current measurements, were obtained from the Rio Grande Pilot Station (Fig. 1b). Wind observations were collected by a Davis Vantage Pro 2 meteorological station, recording at 5-minute intervals and averaged hourly. Water level and current velocity were measured with a moored Sontek Argonaut-XR 1.5 MHz ADCP, deployed at approximately 17 m depth. This instrument recorded 5-minute averaged profiles with a vertical bin size of 1.5 m.

Estimates of freshwater discharge into the Patos Lagoon were also incorporated, based on daily records from the primary tributaries. Discharge data were retrieved from Brazil's National Water Agency (ANA) Hidroweb database (www.snirh.gov.br/hidroweb), using gauge stations from the Jacuí (85900000), Taquari (86720000), Caí (87170000), Sinos (87382000), and Camaquã (87905000) rivers. Additionally, discharge from the São Gonçalo Channel, which connects the Mirim Lagoon to the estuarine system, was provided by the Mirim Lagoon Agency (Agência da Lagoa Mirim – ALM/UFPel). The methodology used to aggregate and estimate river discharge followed the approach described by Santa-Rosa and Schettini (2024).

3.2 Data Analysis

3.2.1 Vessel-mounted ADCP data

The current velocity data recorded by the ADCP were trimmed within 10% of the bottom to remove erroneous data due to side-lobe effects. Velocities greater than 5% of the maximum flow were excluded, and any data ensemble with a signal return

https://doi.org/10.5194/egusphere-2026-1840
Preprint. Discussion started: 23 April 2026

less than 85% good data was removed (Ross et al., 2019). The resulting velocity time series for East-West (u) and North-South (v) components were rotated using principal component analysis (Thomson and Emery, 2014) to align with the longitudinal direction of the flow. For the data recorded in the channel, the decomposition considered two sectors with relatively similar orientation, up to the inlet. Seaward of the inlet, the currents were decomposed into cross-shelf and along-shelf components based on the coastline orientation, determined by two reference points located approximately 10 km on either side of the jetties.

3.2.2 MicroCTD data

The rate of dissipation (ϵ) of TKE is derived from the measurements of velocity shear recorded by the shear probes on the MicroCTD (Lueck et al., 2020). Assuming that the turbulence is isotropic, the TKE dissipation rate is given by:

$$\epsilon = \frac{15}{2}\nu\overline{\left(\frac{\partial u}{\partial z}\right)^2} = \frac{15}{2}\nu\int_0^\infty \Psi(k)dk, \quad (1)$$

where ν is the kinematic molecular viscosity (10^{-6} m^2 s^{-1}), Ψ is the velocity shear spectrum, and k is the wave number (m^{-1}) (Lueck, 2013). This ϵ is expressed as the rate of dissipation of TKE per unit mass (W kg^{-1}, or equally, m^2 s^{-3}) (Thorpe, 2007).

The estimates of ϵ from each of the two shear probes affixed to the instrument were compared at each depth and if the value differed more than a factor of 2, the larger estimate was removed (Stips, 2005). Only two vertical profiles were discarded due to deviations from the operational thresholds of the angle of attack being more than 5° or the descent speed deviating from 0.8 m s^{-1}, representing less than 1.3% of the total casts. Correction for profiler vibration was made using the method of Goodman et al. (2006). Individual wave number spectra for each component were calculated using a Fast Fourier Transform (FFT) with a length of 0.5 m and a time span of 2 s for each estimate of the rate of dissipation. Both calculated ϵ data sets were averaged and then used to quantify the vertical eddy viscosity (A_z). The calculations were done using the Matlab scripts provided by Rockland Scientific, and further pre-processed with Python (Schettini, 2021). Subsequently, all turbulence analysis and the computation of dimensionless stability metrics were performed using a dedicated Python codebase developed for this study (Barros, 2026). This secondary processing stage ensures the reproducibility of the mixing estimates and hydraulic parameters presented hereafter.

3.2.3 Turbulence Parameters and Vertical Mixing

To estimate vertical eddy viscosity (A_z) as a proxy for vertical mixing, the following procedure was adopted. First, along-channel and cross-channel velocity components from each transect were used to calculate the squared vertical shear (S^2), defined as:

https://doi.org/10.5194/egusphere-2026-1840
Preprint. Discussion started: 23 April 2026

$$S^2 = \left(\frac{\partial u}{\partial z}\right)^2 + \left(\frac{\partial v}{\partial z}\right)^2, \quad (2)$$

where u and v are the longitudinal and lateral flow components, respectively, and the coordinate z is positive upward. The buoyancy frequency (N^2) was used to estimate the stratification and is quantified as:

$$N^2 = -\frac{g}{\rho_o}\frac{\partial \rho}{\partial z}, \quad (3)$$

where g is the gravitational acceleration (9.8 m s^{-2}), and ρ_o is a reference density (1025 kg m^{-3}). The stratification stability parameter, also known as the dimensionless gradient Richardson number, is expressed as the ratio of buoyancy frequency to squared vertical shear, $R_i = N^2/S^2$, and was calculated to quantify the influence of stratification on mixing (Monismith, 2010).

From R_i, the flux Richardson number was obtained following Venayagamoorthy & Koseff, 2016, as a scale for mixing efficiency (Holleman et al., 2016; Gregg et al., 2018; Ross et al., 2019):

$$R_f = 0.25\,(1 - e^{-7R_i}). \quad (4)$$

According to Kay and Jay, 2003, in stable stratified flow, R_f is the fraction of total TKE production that is lost to buoyancy, increasing the potential energy of the water column. The mixing coefficient Γ_m is denoted by the mixing efficiency R_f.

$$\Gamma_m = \frac{R_f}{1-R_f}. \quad (5)$$

The vertical eddy viscosity, a proxy of mixing, was calculated as follows (Kay and Jay, 2003; Huguenard et al., 2015; Ross et al., 2019):

$$A_z = \Gamma_m \frac{\epsilon}{S^2}. \quad (6)$$

The buoyancy Reynolds number is calculated as:

$$Re_b = \left(\frac{L_o}{L_k}\right)^{4/3} = \frac{\epsilon}{\nu N^2} \quad (7)$$

https://doi.org/10.5194/egusphere-2026-1840
Preprint. Discussion started: 23 April 2026

where the L_o/L_k is the ratio between the Ozmidov length scale and the Kolmogorov length scale (larger scale over smaller scale of turbulence). The Re_b is a parameter used to indicate the impact of density stratification on turbulence (Barros et al., 2025) and may be referred to in the literature by different names such as the turbulent activity parameter, activity number, strain-based Froude number, Gibson number, or buoyancy Reynolds number (Stacey et al.,1999; Shih et al., 2005; Monismith, 2010; Holleman et al., 2016). The magnitude of Re_b defines distinct regimes in the interaction between buoyancy and turbulence: for $Re_b > 200$, small-scale turbulence is unaffected by stratification; for $15 < Re_b < 200$, the effect of stratification progressively extends to smaller and smaller scales; and for $Re_b < 15$, stratification becomes dominant, resulting in the complete suppression of turbulence (a phenomenon often referred to as 'killing turbulence') (Gargett et al., 1984; Ivey et al., 2008; Monismith, 2010).

3.2.4 Internal Froude Number Calculation

The internal Froude number (Fr_i) is a dimensionless measure of the ratio between inertial and buoyancy forces. It was calculated following (Hetland, 2010; McPherson et al., 2020):

$$Fr_i = \frac{U}{\sqrt{g'h}} \quad (8)$$

where U is the mean velocity of the upper layer relative to the lower layer, and h is the thickness of the low-density surface layer. The term $\sqrt{g'h}$ represents the internal wave speed, where g' is the reduced gravity, defined as $g'=g(\Delta\rho/\rho_0)$.

Determining h requires identifying the pycnocline depth. Within the channel, this was defined by the maximum vertical density gradient ($\partial\rho/\partial z$) for each density profile. In the offshore region, however, the strongest vertical density gradient occurs in the plume layer. The upper layer thickness in the offshore profiles was determined using a profile-shape criterion, defined as the depth at which the density profile transitions from a strongly stratified upper layer (plume) to a nearly homogeneous underlying water mass (coastal water). This approach identifies the base of the buoyant plume while avoiding spurious detection of near-surface gradients.

The flow regime is considered subcritical if $Fr_i < 1$, indicating that buoyancy forces dominate over inertia (potential energy dominance). In this state, stratification is strong, and internal waves can propagate upstream; the plume tends to be stable and spread horizontally (Nash and Moum, 2005; Hetland, 2010). Conversely, if $Fr_i > 1$, the flow is supercritical, meaning inertial forces dominate (kinetic energy dominance). In this regime, stratification is insufficient to constrain the flow, potentially leading to turbulent mixing and density jumps (Horner-Devine et al., 2015; Geyer et al., 2017). A hydraulic jump may occur

https://doi.org/10.5194/egusphere-2026-1840
Preprint. Discussion started: 23 April 2026

during an abrupt and turbulent transition where the flow shifts from a supercritical to a subcritical state (Dorrell et al., 2016; Thorpe et al., 2017).

3.2.5 Channel Morphology

In order to understand the influence of channel morphology on the measured and derived variables, cross-sectional areas along the channel were calculated. The inner channel was divided into 57 cross-sections, and the area of each section was estimated by constructing a closed polygon bounded above by the water surface and below by a high-resolution bathymetric survey conducted in 2024 using a single-beam echosounder and DGPS positioning (Fig. 1b).

For each section, a reference line was defined between two control points, and all bathymetric data within a lateral buffer of ±50 meters from this line were considered. To project the bathymetric points onto the local reference frame of the transect, each point (x, y) was expressed in terms of its longitudinal ($d_{\parallel}$) and perpendicular ($d_{\perp}$) distances:

$$d_{\parallel} = (x - x_0).u_x + (y - y_0).u_y \quad (9)$$

$$d_{\perp} = \left|(x - x_0)(-u_y) + (y - y_0)u_x\right| \quad (10)$$

where (x_0, y_0) is the starting point of the transect, and (u_x, u_y) is the unit vector in the direction of the transect. Points satisfying $0 \le d_{\parallel} \le L$ and $d_{\perp} < 50$ meters (with L being the transect length) were retained for area calculation.

The bathymetric profile was ordered along the transect axis to form the lower boundary of the polygon, while the water surface was assumed to be locally horizontal and defined by a straight line between the transect endpoints. This assumption is reasonable for short cross-sections and allows the area to represent a first-order approximation of the wet section at the time of sampling. The polygon was constructed by concatenating the surface line with the reversed bathymetric profile.

4 Results

4.1 Environmental Conditions and Inner Channel Dynamics (The Transect Segment)

The environmental conditions during the survey favoured the outflow of lagoon waters and the formation of a buoyant plume. To characterize this state, the river discharge of the main tributaries, along with water level, wind vectors in meteorological convention, and current velocities measured in the channel at the Pilot's Station (Fig. 1b) during the days preceding the survey,

https://doi.org/10.5194/egusphere-2026-1840
Preprint. Discussion started: 23 April 2026

are shown in Figure 2. On the day of the fieldwork (18 July 2022), the gauged river discharge was approximately 6,900 $m^3 s^{-1}$ (Fig. 2a), which is significantly higher than the estimated average flow of 3,707 $m^3 s^{-1}$ for the same month.

The gauged river discharge represents the freshwater inflow to the lagoon; however, it does not necessarily correspond to the discharge at the lagoon mouth due to storage, mixing, and exchange processes within the lagoon (Santa Rosa and Schettini, 2024). The total discharge at the lagoon mouth, measured across the Transect segment, reached 9,400 $m^3 s^{-1}$, with an average salinity of 6 g kg^{-1} (Fig. 3b). Using the observed coastal salinity during the survey (~ 28 g kg^{-1}) as a reference, the freshwater discharge was estimated at 7,650 $m^3 s^{-1}$. The difference between the gauged river discharge and the actual freshwater flow at the lagoon's mouth can be attributed to wind-driven water level variations along the lagoon and the residence time of water parcels within the system.

Water level variability during the survey was minimal, fluctuating by approximately 0.20 m (Fig. 2b). Wind speeds were relatively weak compared to the preceding days (Fig. 2c), blowing from NNW to W and ranging between 1.8 and 5.4 m s^{-1}. The current flowed seaward throughout the entire water column during the fieldwork (Fig. 2d), with velocities ranging from 0.8 m s^{-1} near the bottom to 2.2 m s^{-1} near the surface, without reversal. These results from the moored ADCP corroborate the Transect observations (Fig. 3a), showing outflow across the entire water column, with higher velocities of approximately 2 m s^{-1} concentrated at the surface and along the main axis of the channel. Nevertheless, this condition represented a significant variation compared to the previous days in the interval, during which the current had been flowing in the opposite direction due to the passage of a frontal system with up-estuary winds. This high-discharge, outflow-dominated state provides the boundary conditions for the plume development analysed in the following section.

https://doi.org/10.5194/egusphere-2026-1840
Preprint. Discussion started: 23 April 2026

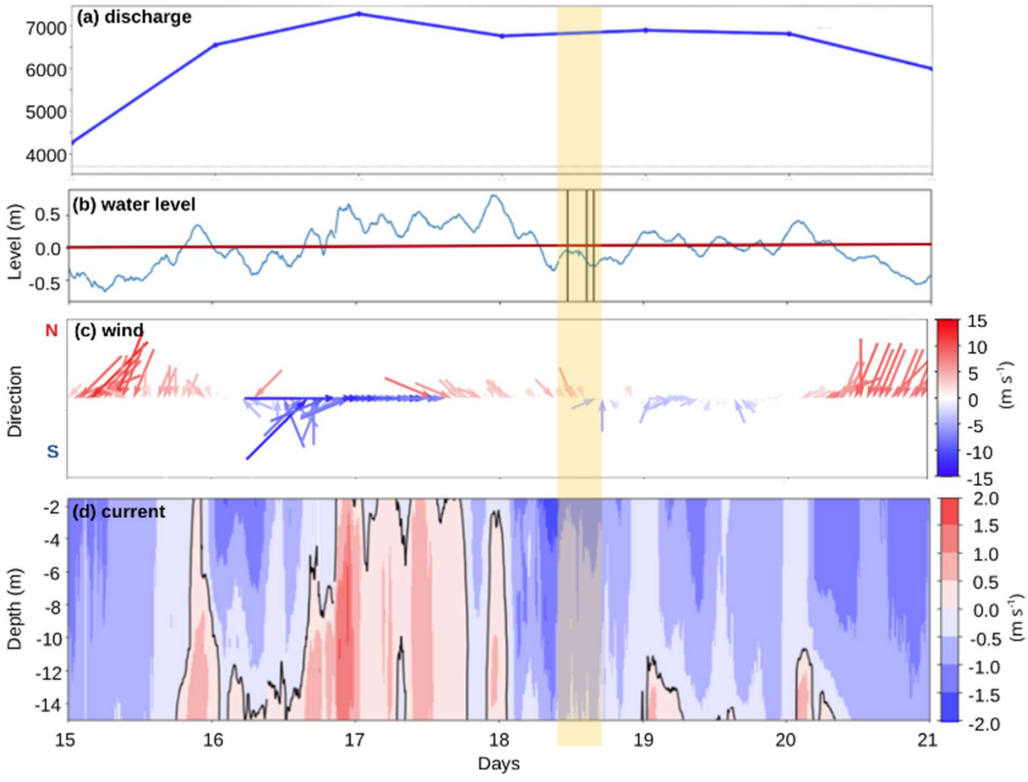

Figure 2: Environmental conditions between 15 and 21 July 2022, with the vertical yellow bar representing the survey period. **(a)** Gauged river discharge of the Patos Lagoon (m^3 s^{-1}), **(b)** Water level (m) measured in the channel, where the three vertical lines indicate the start moment of each section: Drift, Jetties, and Transect. **(c)** Vector plot of wind velocity (m s^{-1}) in meteorological notation, where blue represents southerly winds (blowing towards the north) and red represents northerly winds (blowing towards the south). **(d)** Hovmöller diagram of the along-channel current velocity (m s^{-1}) measured in the channel, where red indicates inflow (flood) and blue indicates outflow (ebb).

https://doi.org/10.5194/egusphere-2026-1840
Preprint. Discussion started: 23 April 2026

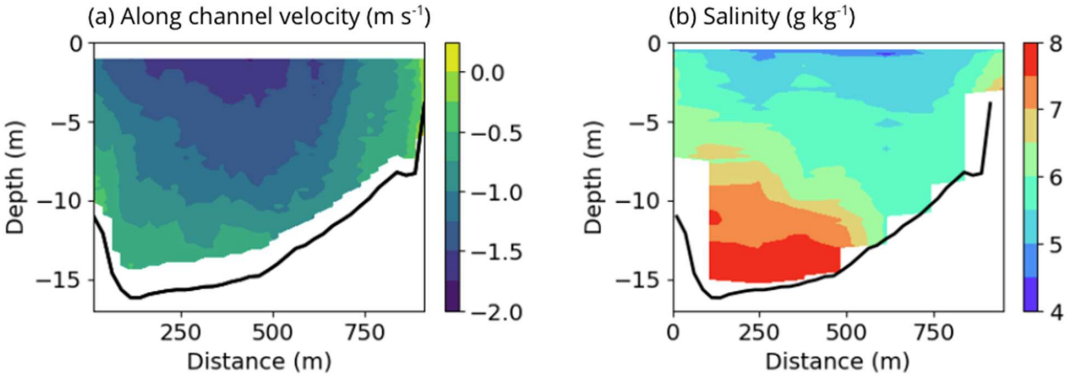

Figure 3: Cross-sectional distribution of **(a)** along channel current velocity (m s^{-1}; negative values indicate outflow) and **(b)** salinity (g kg^{-1}) at the Transect segment, characterizing the lagoon outflow during the survey.

4.2 Estuary–Shelf Transition and Near-Field Plume (The Drift Segment)

The spatial distributions along the Drift segment are presented in scatter plot diagrams, where vertical profiles feature a 0.5 m resolution and horizontal positioning corresponds to each cast's location. This graphical representation underscores the extensive sampling density achieved during the campaign and allows for the identification of spatial coherence between neighbouring profiles. Such high-resolution visualization is particularly relevant for properties with strong spatial variability, such as TKE dissipation (ϵ) and the Richardson number (R_i), ensuring that the observed structures reflect genuine physical features captured at the sampling sites.

4.2.1. Water Mass Characterization and Vertical Structure

The spatial distribution of temperature, salinity, and density across the Drift segment illustrates the horizontal and vertical development of the estuarine plume as it exits the channel. Within the channel (distance ≤ ~8.5 km), salinity (Fig. 4a) ranged from 7 to 13 g kg^{-1}, with a relatively clear vertical distinction at the density interface (black dashed line in Fig. 4a-c). In the outer region (distance ≥ ~8.5 km), vertical variability intensifies, with values spanning 7 to 28 g kg^{-1} near the mouth, followed by a gradual increase in surface salinity as the plume disperses offshore. Temperature (Fig. 4b) shows less variability than salinity (< 1°C) but remains consistent with salinity patterns. Consequently, the density distribution (Fig. 4c) closely mirrors salinity, ranging from 1005 to 1021 kg m^{-3}.

https://doi.org/10.5194/egusphere-2026-1840
Preprint. Discussion started: 23 April 2026

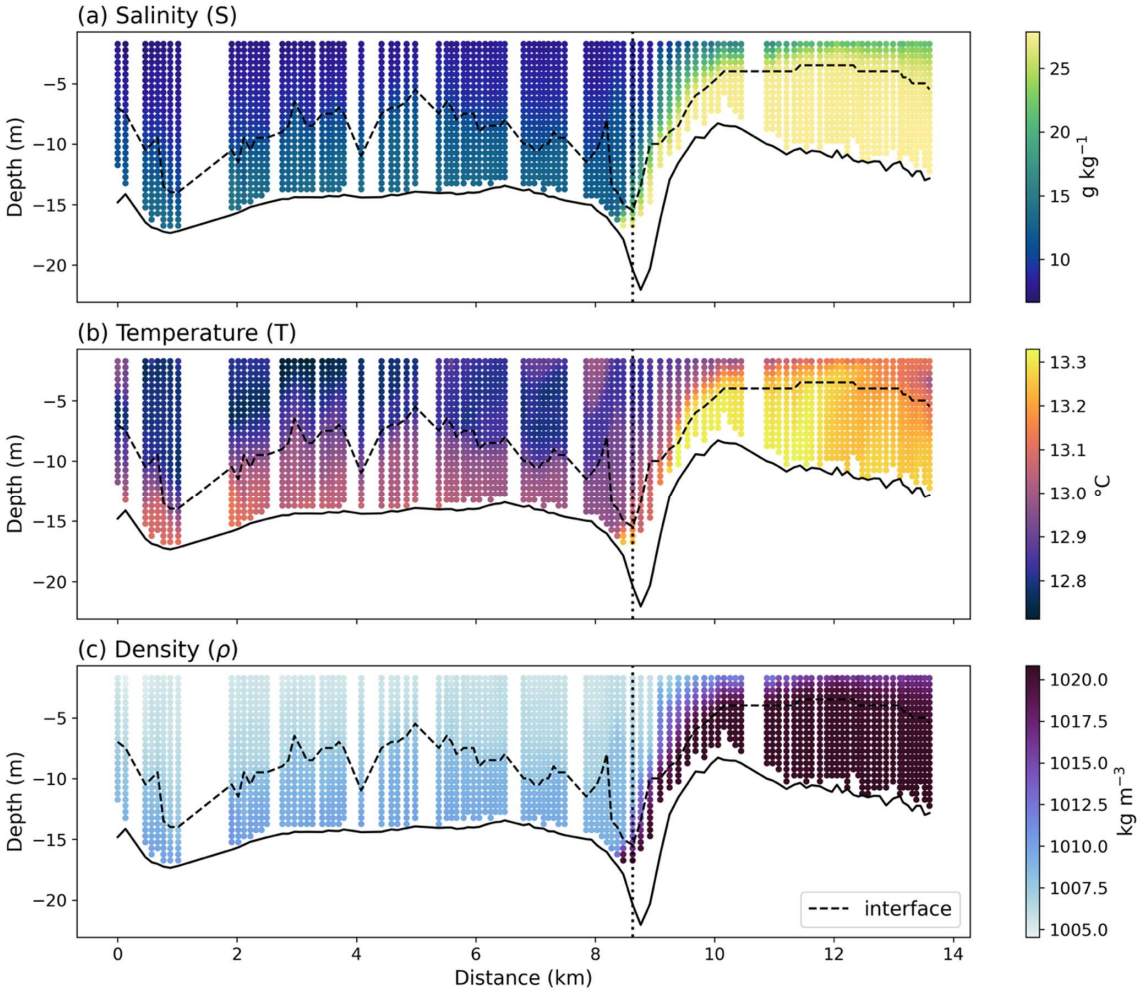

Figure 4. Spatial distributions of **(a)** salinity (g kg^{-1}), **(b)** temperature (ºC), and **(c)** density (kg m^{-3}). The dashed line indicates the interface position between layers. The vertical dotted line marks the position of the mouth (inlet). Distance (km) is measured from the first upstream profile within the channel.

The transition from the laterally constrained channel flow to the unconstrained shelf environment is marked by significant morphological changes and baroclinic adjustments (Chao and Boicourt, 1986; Valle-Levinson et al., 1996). The T-S diagram (Fig. 5) illustrates the thermohaline structure resulting from these adjustments and the subsequent mixing stages of the sampled waters, distinguishing the inner region (warm tones) from the outer region (cold tones), with colour shading indicating depth.

https://doi.org/10.5194/egusphere-2026-1840
Preprint. Discussion started: 23 April 2026

The distribution reveals three primary water masses: (i) low-salinity (< 15 g kg^{-1}), representing estuarine water influenced by river discharge and meteorological forcing; (ii) an intermediate salinity range (15–27 g kg^{-1}), reflecting active mixing between estuarine and coastal waters; and (iii) high-salinity (> 27 g kg^{-1}), representing relatively homogeneous coastal water.

The low-salinity partially mixed estuarine water (< 15 g kg^{-1}) is composed of two main branches: the first with a vertical shape (yellow, with salinity < 8 g kg^{-1}) represents near-surface estuarine water, while the second (red, with salinity ranging from 8 to 15 g kg^{-1}) exhibits a diagonal trend, representing the deeper estuarine layer. The intermediate mixing region (majority of blue points, 15-27 g kg^{-1}), shows the data also along a well-defined diagonal trend, reflecting coupled variations in temperature and salinity and thus active conservative mixing between estuarine and coastal waters, representing the plume waters over the shelf. At higher salinities, the distribution becomes more vertically clustered again (purple cluster, > 27 g kg^{-1}), representing a second, relatively homogeneous water mass associated with coastal waters. This most saline and deeper water represents the regional coastal water under the influence of the La Plata River plume, a buoyant coastal current that flows northward along the southwestern Atlantic shelf and episodically reaches the study area, modulating the thermohaline structure of the adjacent coastal waters, particularly during winter (Campos et al., 2008).

The geometry of these branches indicates the nature of the mixing processes (Miranda et al., 2002). Additionally, the marginal histograms (Fig. 5) highlight the sampling density, where the bimodal salinity distribution underscores the clear separation between the estuarine core and the coastal water. In contrast, the more continuous temperature distribution, given its relatively small range (~ 0.6 °C) reflects the subtle thermal gradient across the plume, confirming that density remains primarily salinity-driven in this near-field region.

https://doi.org/10.5194/egusphere-2026-1840
Preprint. Discussion started: 23 April 2026

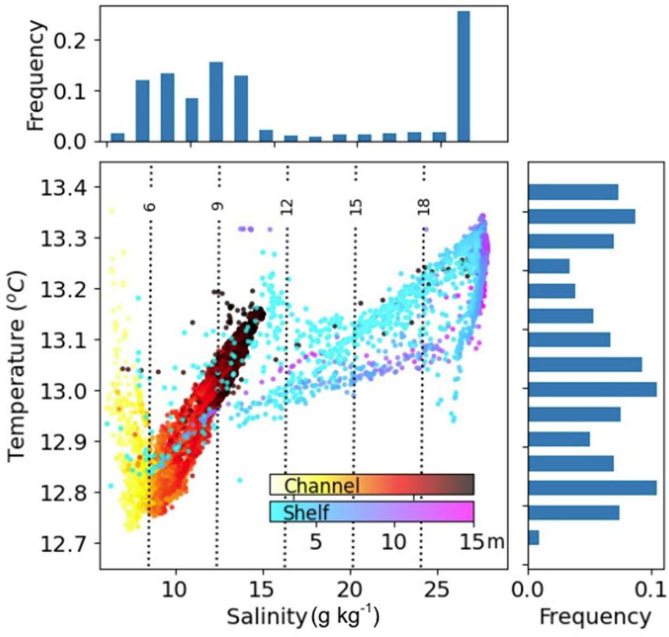

Figure 5. Temperature–Salinity (T–S) diagram and frequency histograms of salinity (top) and temperature (right) for the Drift segment. The central panel shows temperature (°C) versus salinity (g kg^{-1}), with dotted vertical lines indicating density anomaly (σ_t) values of 6, 9, 12, 15, and 18 kg m^{-3} (referenced to 1000 kg m^{-3}). The colour bar distinguishes data from the Channel (warm tones) and the Shelf (cold tones), with shading representing the sampling depth (m).

The high-resolution vertical density profiles exhibit the structural evolution of the water column across the channel-to-shelf transition (Fig. 6). Within the channel (red-toned lines), profiles are clustered between 1005 and 1010 kg m^{-3}, with relatively weak vertical density gradients, especially when compared to other conditions in the same system (Barros et al., 2025), indicating a partially mixed water column. As the flow exits the jetties into the shelf (blue-toned lines), a sharp two-layer stratification emerges. In this outer region, surface density increases to 1012-1021 kg m-3, while the pycnocline rises and stabilizes at depths shallower than 5 m. Below this interface, density converges to values between 1020 and 1021 kg m^{-3}. This transition from a less stratified channel flow to a more strongly stratified near-field plume provides the physical context for the flow and mixing results presented next.

https://doi.org/10.5194/egusphere-2026-1840
Preprint. Discussion started: 23 April 2026

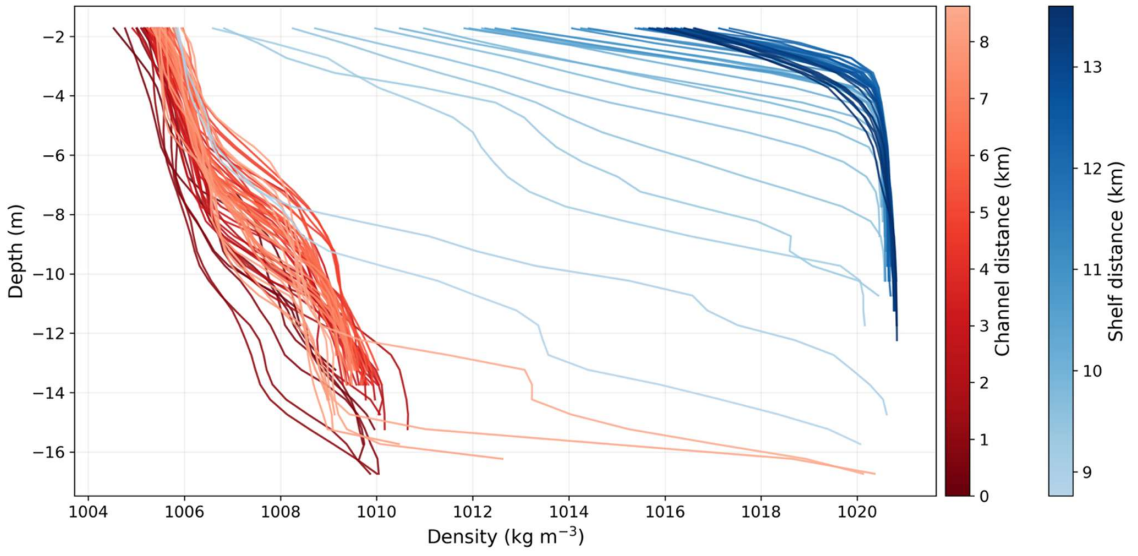

Figure 6. Vertical density profiles (kg m^{-3}) across the channel-to-shelf transition. Lines are colour-coded by distance (km) from the starting point of the drift segment. Red tones represent profiles within the inner channel (0-8.5 km) and blue tones represent profiles in the shelf region (9-13.5 km).

4.2.2. Flow Dynamics and Velocity Structure

The longitudinal velocity component (Fig. 7a) shows a predominantly seaward-directed (negative) flow throughout the entire water column, with higher velocities at the surface (up to ~1.8 m s^{-1}) that decrease with depth. A vertical gradient of the along-channel velocity occurs at the interface between the two density layers, indicated by the dashed line in Fig. 7a. Although this observation is subtle in the velocity data alone, it becomes more evident when viewed alongside the water property observations (Fig.4). However, beyond the inlet (km 8.5), this vertical gradient becomes more pronounced. The intensity of the outflow in the upper layer intensifies, exceeding 2.0 m s^{-1} just after the mouth at the estuary–ocean connection. The upper layer loses momentum as its thickness increases farther offshore (beyond km 11), while moving away from the source region. Below the interface, the velocity is significantly lower (typically < 0.5 m s^{-1}, representing less than 25% of the surface magnitude) and a flow reversal (positive values) occurs near the bottom in the outermost portion.

The cross-channel velocity component (Fig. 7b) within the inner channel exhibits magnitudes ranging from -0.51 to 0.41 m s^{-1}, reflecting a flow primarily aligned with the longitudinal axis. These lateral flow patterns change direction (shifting between

https://doi.org/10.5194/egusphere-2026-1840
Preprint. Discussion started: 23 April 2026

positive and negative values) across the water column, especially along the layer interface, particularly in the region of highest constriction (approx. km 8). Once on the shelf (beyond km 9), the cross-shelf signal becomes dominant, reaching magnitudes of -0.68 m s^{-1} and showing consistency throughout the water column. This shift reflects that, once outside the channel's confinement, the plume's lateral flow responds mainly to shelf forcing, whereas the inner channel circulation reflects local morphological adjustments.

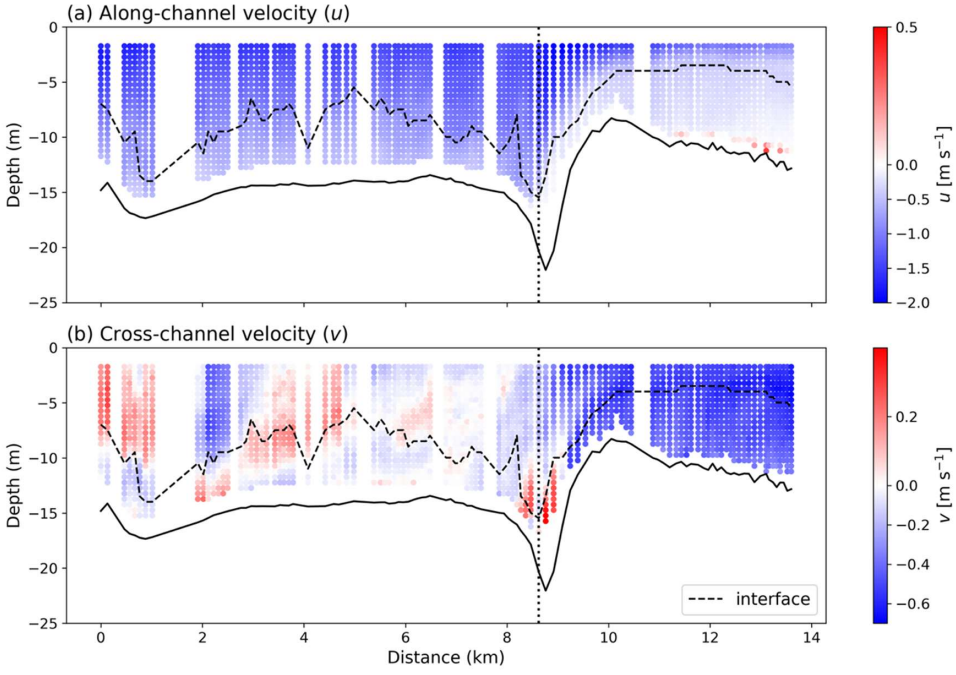

Figure 7. Spatial distributions of **(a)** along-channel and **(b)** cross-channel velocity components (m s^{-1}) synchronized with the MicroCTD profiles. The dashed line indicates the interface position between layers. The vertical dotted line marks the position of the mouth (inlet). Distance (km) is measured from the first upstream profile within the channel.

4.2.3. Turbulent Regimes and Stability Parameters

The turbulent kinetic energy dissipation rate (ϵ) along the section is presented in Figure 8. The values of ϵ vary across four orders of magnitude, ranging from 10^{-7} to 10^{-3} W kg^{-1}. The highest values were recorded in the region immediately following the mouth (km 9-10) throughout the entire water column. This zone of high dissipation extends offshore within the surface layer above the interface. Below the interface on the shelf, dissipation values were relatively lower (10^{-6} W kg^{-1}). The lowest

https://doi.org/10.5194/egusphere-2026-1840
Preprint. Discussion started: 23 April 2026

dissipation values (< 10^{-7} W kg^{-1}) were recorded within the channel in the mid-water column between km 5 and 7, in the vicinity of the density interface. This zone corresponds to the wider section that precedes the narrowing of the jetties towards the mouth.

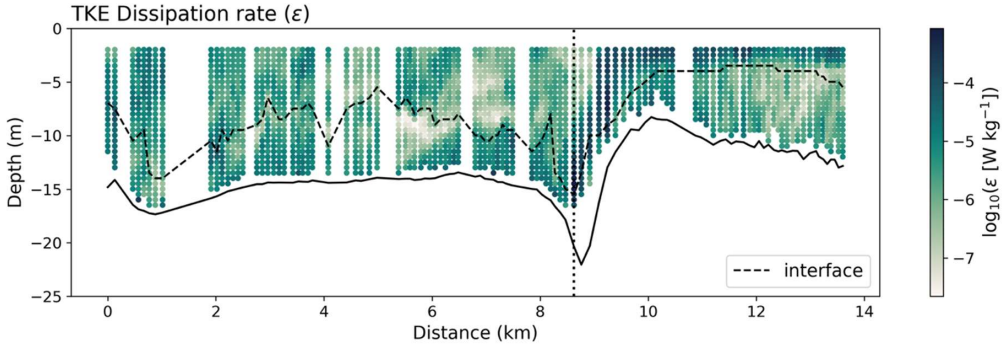

Figure 8. Spatial distribution of the turbulent kinetic energy dissipation rate (ϵ, log10(W kg^{-1})). The dashed line indicates the interface position between layers. The vertical dotted line marks the position of the mouth (inlet). Distance (km) is measured from the first upstream profile within the channel.

The spatial distributions of buoyancy frequency (N^2) and squared vertical shear (S^2), and the gradient Richardson (R_I) are presented in Figure 9. The buoyancy frequency (Fig. 9a) shows lower variability along the channel, with higher values coinciding with the pycnocline (interface). On the shelf, a more intense vertical gradient is observed between the surface layer, presenting higher values (~10^{-1} s^{-2}), and the bottom layer (~10^{-5} s^{-2}). The spatial distribution of the squared vertical shear (Fig. 9b) is relatively consistent with the N^2 patterns. The highest S^2 values also occur at the transition between the inlet and the shelf, as well as within the shelf's surface layer (~10^{-1} s^{-2}). The largest S^2 values in the channel were co-located with the pycnocline.

The gradient Richardson number, R_i, was rescaled as log10(R_i /0.25), such that positive values reflect $R_i > 0.25$ and negative values reflect $R_i < 0.25$ (Fig. 9c), where Ri ≈ 0.25 represents a classical threshold below which stratified shear flows become susceptible to instability (Miles, 1961). Within the inner region of the inlet, values below 0.25 are predominantly concentrated in the surface layer, while values above this threshold occur especially around the interface. Near the mouth (vicinity of km 8.5), nearly the entire water column exhibits values above 0.25, forming a stable vertical barrier. In the outer region, a vertical decoupling is observed where the surface plume and the near-bottom layer present values below 0.25, whereas a persistent layer of values above 0.25 follow the stratified interface region, effectively isolating the plume from the deeper shelf waters.

https://doi.org/10.5194/egusphere-2026-1840
Preprint. Discussion started: 23 April 2026

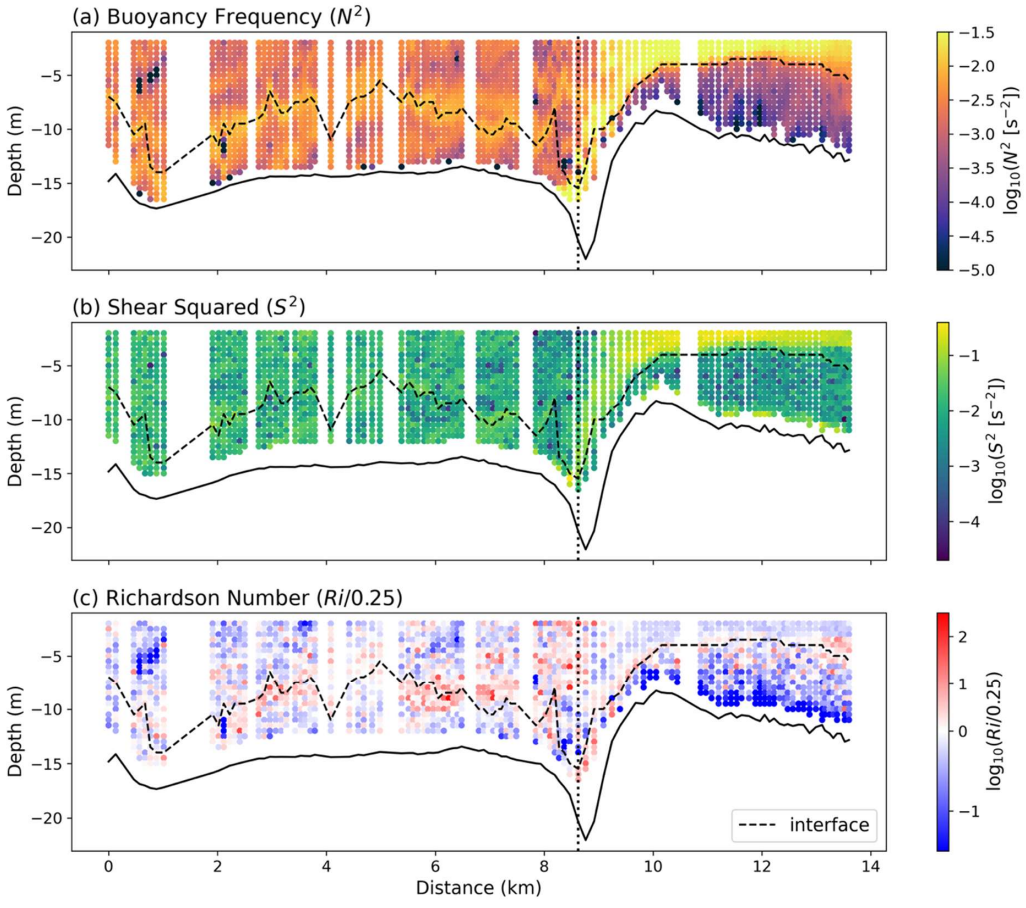

Figure 9. Spatial distributions of **(a)** buoyancy frequency (N^2, s^{-2}), **(b)** squared vertical shear (S^2, s^{-2}), and **(c)** gradient Richardson number normalized by its critical value (R_i/0.25). The dashed line indicates the interface position between layers. The vertical dotted line marks the position of the mouth (inlet). Distance (km) is measured from the first upstream profile within the channel.

The spatial distributions of the vertical eddy viscosity (A_z) and the buoyancy Reynolds number (Re_b) are presented in Figure 10. The vertical eddy viscosity exhibits values ranging from 10^{-6} to 10^{-1} m^2 s^{-1}, showing significant vertical and longitudinal variability along the section (Fig. 10a). The lowest values occur primarily in the mid-water column between km 5 and 7. In contrast, the highest values are found near the seabed on the shelf, adjacent to the mouth at km 9.

The buoyancy Reynolds number was calculated as an indicator of the degree to which stratification suppresses turbulence. High Re_b values are observed throughout most of the channel (Fig.10b), particularly in the region between km 9 and 10, where

https://doi.org/10.5194/egusphere-2026-1840
Preprint. Discussion started: 23 April 2026

values remain above 200 over the water column. Values between 15 and 200, which indicate that stratification is actively constraining turbulence, are specifically found in the mid-water column between km 5 and 7.5, as well as along the density interface in the channel, and near the offshore end of the section (km 13). Values lower than 15 appear at isolated points along the interface, with a notable cluster occurring within the pycnocline between km 5 and 7.5, which indicate that stratification is fully suppressing turbulence at these locations.

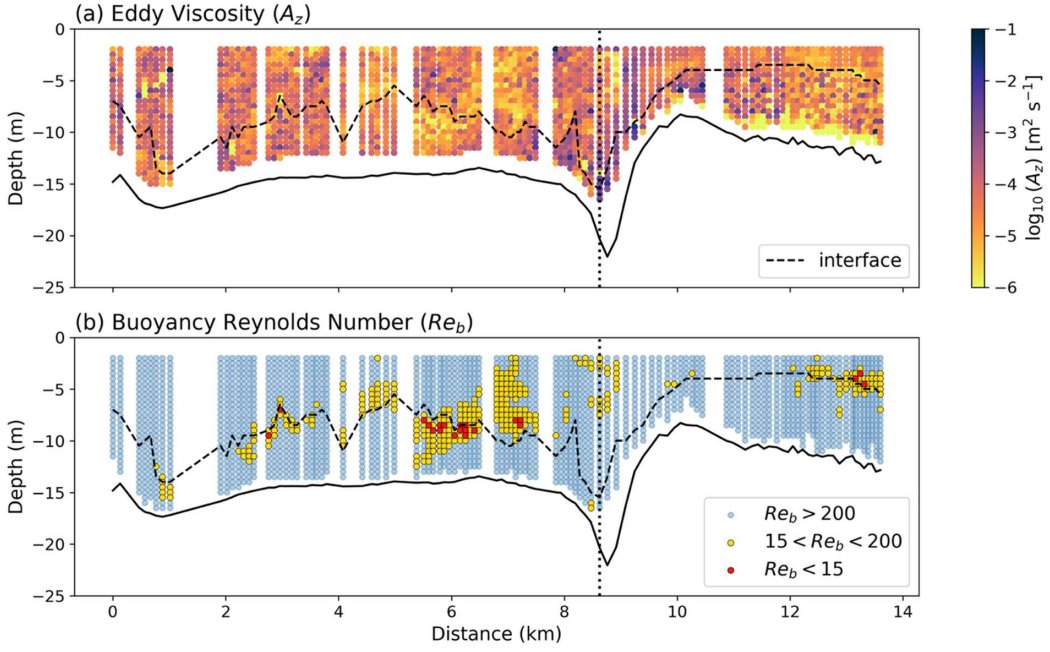

Figure 10. Spatial distributions of **(a)** the vertical eddy viscosity (A_z, m^2 s^{-1}), and **(b)** the buoyancy Reynolds number (Re_b). The dashed line indicates the interface position between layers. The vertical dotted line marks the position of the mouth (inlet). Distance (km) is measured from the first upstream profile within the channel.

4.3 Adjacent Inner Shelf Baseline (the Jetties Segment)

To contextualize the magnitude of the turbulence observed within the plume, the vertical profiles conducted in the Jetties segment serve as a baseline reference for the adjacent inner shelf. Compared to the high-velocity jet observed in the Drift segment, the current velocity profiles at the Jetties segment (Fig. 11a) exhibit distinctly lower magnitudes and greater vertical uniformity, averaging to approximately 0.2 m s^{-1}. Nevertheless, the upper layer at Station 1 (green line), which is the outermost

https://doi.org/10.5194/egusphere-2026-1840
Preprint. Discussion started: 23 April 2026

(most seaward) location, exhibited larger variations, reaching over 0.4 m s^{-1} at the surface. This behaviour is consistent with the density profiles (Fig. 11b), which indicate a more stratified water column at Station 1 compared to moderate stratification at Station 2 (blue line). Conversely, Station 3 (yellow line), which is located closest to shore, exhibits a nearly vertical density profile, indicating a well-mixed water column with no apparent pycnocline.

Under these conditions, the TKE dissipation rates (ϵ) at these stations (Fig. 11c) are significantly lower than those recorded in the main plume axis, ranging between 10^{-8} and 10^{-6} W kg^{-1}, with the minimum values occurring mid-water column, just below the pycnocline at each station. This is even the case for station 3, which has a nearly uniform density profile, although the values of ϵ are up to a magnitude smaller than the other two stations. Furthermore, Az fluctuates between 10^{-5} and 10^{-3} m^2 s^{-1} without a specific vertical pattern (Fig. 11d). The reduced velocities and relative uniformity, combined with the markedly lower stratification and dissipation at these reference points, confirm that the intense turbulent activity described in the Drift segment is an intrinsic process of the plume dynamics rather than a general characteristic of the inner shelf. This contrast highlights the unique turbulent signature of the plume, where internal structures are governed by localized mixing processes at the estuary–shelf interface.

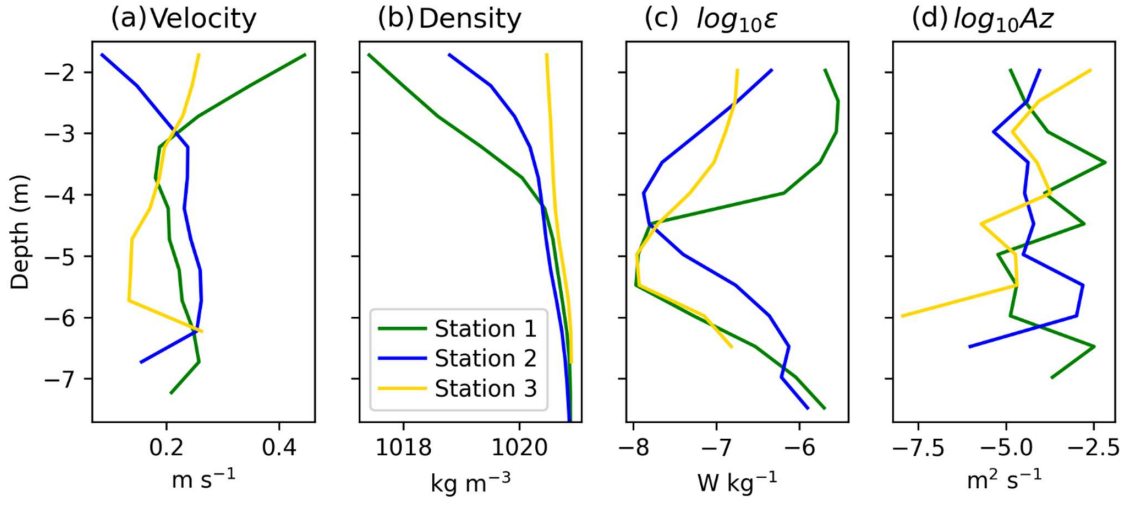

Figure 11. Vertical profiles of **(a)** current velocity (u, m s^{-1}), **(b)** water density (ρ, kg m^{-3}), **(c)** TKE dissipation rate (ϵ, W kg^{-1}), and **(d)** vertical eddy viscosity (A_z, m^2 s^{-1}) at the three baseline stations in the Jetties segment. Green, blue, and yellow lines represent Stations 1 (outermost), 2 (intermediate), and 3 (innermost), respectively. The x-axis tick labels in panels (c) and (d) indicate the logarithmic exponents.

https://doi.org/10.5194/egusphere-2026-1840
Preprint. Discussion started: 23 April 2026

5 Discussion

5.1. Representative Snapshot and Forcing Dominance

The field data were collected over a 5-hour window, from the beginning of the Drift segment (11:21 LT) to the completion of the Transect (16:30 LT). Despite the time elapsed between surveys, these results represent a quasi-synoptic snapshot of the hydrodynamic conditions. In estuarine environments where astronomical tides are dominant, sampling designs must strictly adhere to hourly variations to capture tidal phases (Dyer, 1979; Kjerfve, 1990). However, in the Rio Grande Channel, astronomical tides play a secondary role, accounting for less than 20% of the current variance (Santa-Rosa and Schettini, 2024). As established by the spectral characterization for July 2022 (Barros et al., 2025), the system is dominated by low-frequency energy (periods > 25 h) associated with synoptic frontal systems.

This meteorological dominance ensured a quasi-synoptic state during the survey, characterized by minimal water level fluctuations (< 0.20 m; Fig. 2b) and a persistent, uniform ebb-directed flow (Fig. 2d). Such stationarity validates the comparison of data across different sampling moments, allowing the analysis to move beyond temporal variability and focus on the spatial processes and internal plume structure that define the estuary-shelf transition.

5.2. Morphological Control and Multi-regime Dynamics

The spatial distribution of the TKE dissipation rate (ϵ) along the drift segment highlights a clear maximum near the mouth and within the buoyant plume's surface layer. These high values align with the plume's 'lift-off' zone (MacDonald and Geyer, 2004) and exhibit a decay proportional to the distance from the inlet (O'Donnell et al, 2008; McPherson et al., 2019). This maximum dissipation zone, associated with the plume's evolution over the quiescent coastal water, follows expected theoretical patterns for near-field river plumes (Horner-Devine et al., 2015).

Considering the internal channel dynamics a high degree of coupling with the local morphology is observed (Fig. 12). This contrasts with the finding of Barros et al. (2025), collected in the same study area with a 24 h difference (July 19th, 2022), where the presence of a salt wedge and a strong pycnocline acted to decouple the surface flow from the bottom topography and suppress turbulence. However, the present study (July 18th, 2022; Fig. 2) captures a fully flushed, inertia-dominated state, which shows peak discharge conditions that exhibit a more direct response to topographic control.

Within the channel, the localized decrease in ϵ (between ~ km 4 and 7) directly corresponds to the expansion of the cross-sectional area, which redistributes kinetic energy and reduces local shear. As the flow approaches the final constriction near the mouth (km 8.5, dashed line), the abrupt reduction in cross-sectional area forces a convergence that drives current velocities

https://doi.org/10.5194/egusphere-2026-1840
Preprint. Discussion started: 23 April 2026

to their maximum, resulting in the absolute peak of ϵ on the order of 10^{-3} W kg^{-1}. In this specific case, the morphological forcing is sufficient to overcome the vertical stability, triggering the intense mixing observed at the estuary–shelf interface.

Once the flow exits the jetties and enters the shelf, a reduction in ϵ is recorded (Fig. 12). Although the buoyant plume remains vertically restricted to the upper layer (Fig. 4a, c), the total loss of lateral confinement allows for a rapid horizontal spread. This transition from a topographically constrained jet to an unconfined plume leads to a significant decay in kinetic energy, marking the end of the high-energy near-field regime.

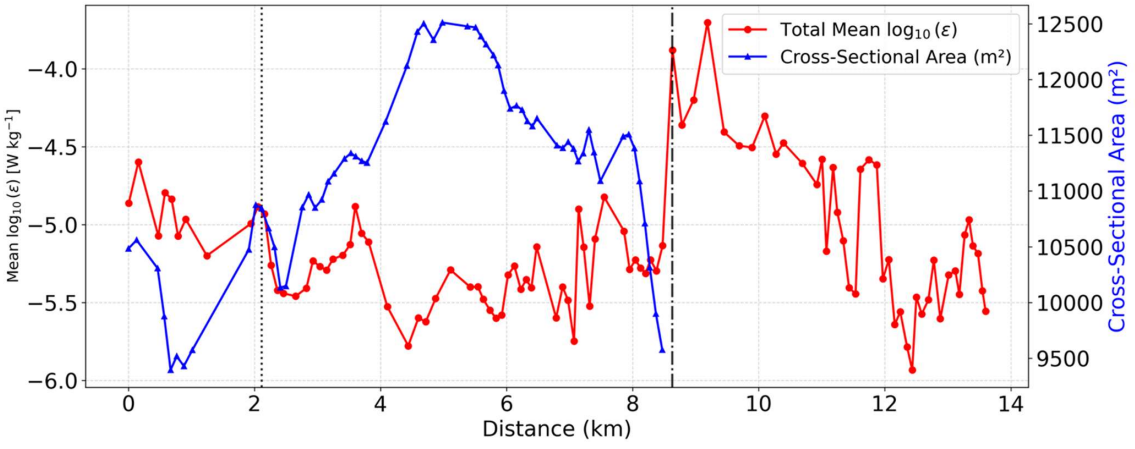

Figure 12. Longitudinal distribution of depth-average TKE dissipation rate (log 10 (ϵ), W kg^{-1}) and channel cross-sectional area (m^2) as a function of distance. The red line (left Y-axis) represents the average dissipation rate, while the blue line (right Y-axis) indicates the cross-sectional area along the Drift segment. The dotted vertical line marks the initial channel widening, and the dash-dotted vertical line indicates the maximum constriction point (mouth) at the estuary–shelf interface.

The rapid transition between the morphology-dominated state described here and the stratification-dominated regime observed on the following day (Barros et al., 2025) highlights that the Patos Lagoon inlet operates under a highly complex non-stationary regime.

The observations presented here record the peak of a discharge event triggered by the relaxation of a meteorological sea-level set-up. As shown in Fig. 2d, the preceding landward wind stress promoted an inward water accumulation within the lagoon; once this forcing ceased, the resulting pressure gradient drove seaward flushing. This mechanism is a recurrent feature of the system's sub-tidal dynamics, where the passage of frontal systems every 5–7 days dictates the alternation between extreme outflow and salt-wedge intrusion (Möller et al., 2001; Fernandes et al., 2005).

https://doi.org/10.5194/egusphere-2026-1840
Preprint. Discussion started: 23 April 2026

These results suggest that in such microtidal environments, the temporal variability of mixing and turbulence is governed more by synoptic-driven events than by the predictable tidal cycle. The rapid shift observed here, from an inertia-dominated 'flushed' state to a stratified 'salt-wedge' intrusion state within only one day, highlights the importance of high-resolution spatial surveys to capture these transient regimes. In this context, the reduced tidal influence represents a key advantage, as it allows the isolation of wind-, discharge-, and morphology-driven processes that are often masked in strongly tidal systems. Therefore, these observations provide a useful framework for understanding the turbulent dynamics of estuarine–shelf systems, not only in microtidal environments but also in more complex settings where multiple forcings interact.

5.3. Hydraulic Regime and Internal Froude Number Analysis

Considering the hydrodynamic transition along the Drift segment, the potential for an internal hydraulic jump was investigated. Based on the vertical density distribution and layer-averaged velocities (Fig. 13a-c), the internal Froude number (Fr_i) was calculated to characterize the flow's criticality (Fig. 13d). Such phenomena are common in estuarine plumes where the flow transitions from a supercritical ($Fr_i > 1$) to a subcritical ($Fr_i < 1$) regime. These transitions are often interpreted through idealized models of internal hydraulic jumps, though their application to natural, high-energy flows requires careful consideration of mixing and layer entrainment (Thorpe et al., 2017).

Despite indicators of intense changes in plume velocity and thickness and interfacial mixing (Fig. 7 and Fig. 8), the results show that the system remained persistently supercritical throughout the entire Drift segment (Fig. 13). Inertial forces heavily dominated this system during the sampling period. High surface velocities (~ 2 m s^{-1}) resulted in elevated Fr_i values, as the flow's momentum far outweighed the stabilizing effect of buoyancy, even under sharp stratification. This persistent supercriticality along the main axis is consistent with flow dynamics observed in energetic channel-to-plume transition zones, where high inertia and high-velocity discharge prevent immediate hydraulic adjustment to subcritical conditions (Dorrell et al., 2016).

Such momentum implies that the flow is too rapid for internal disturbances to propagate upstream (Nash and Moum, 2005). This observed vertical structure, which is characterized by a thin, high-velocity surface layer over a saltier ambient water mass, follows the conceptual model of strongly stratified river plumes documented in large-scale systems (Nash et al., 2009). While the supercritical flow blocks the upstream migration of internal waves, the intense velocity gradient it creates is precisely what triggers localized mixing. The strong shear at the plume's base may promote Kelvin-Helmholtz (KH) instabilities, which drive the recorded peaks in ϵ, a process consistent with observations in other highly stratified discharge regions (e.g., Spicer et al., 2022).

https://doi.org/10.5194/egusphere-2026-1840
Preprint. Discussion started: 23 April 2026

The absence of a hydraulic jump may indicate that the transition to a subcritical regime likely occurs further offshore. This is supported by the progressive decrease in velocity, the deepening of the surface layer interface (McPherson et al., 2020), and the downward trend of Fr_i observed towards the offshore end of the Drift segment, particularly beyond km 12 (Fig. 13). The persistence of this supercritical state for several kilometres is a known feature of river plumes where the buoyant layer spreads laterally upon entering the ocean (Hetland, 2010; Horner-Devine et al., 2015). In these cases, the lateral straining of the shear layer acts as a sustained forcing mechanism for mixing, consistent with the elevated TKE values found in this region (Fig. 8), delaying the transition to a subcritical state until significant interfacial entrainment and expansion occur (Geyer et al., 2017).

The results indicate that the entire sampled domain (km 0 to 13) remains within the near-field as defined by Jirka et al. (1981), given that the system did not transition to a subcritical regime ($Fr_i > 1$ throughout). However, adopting the more detailed classification of Horner-Devine et al. (2015) allows for a finer distinction of the plume's evolution. The region up to the mouth (km 8.5) corresponds to the source region, where flow is governed by estuarine momentum and geometry. Beyond this point, despite the onset of lateral expansion and intense interfacial mixing (Fig. 8), the plume transitions into the buoyancy-forced region, while remaining persistently supercritical.

No evidence of a transition to the mid-field region, typically associated with reduced inertial dominance and a shift toward subcritical conditions, is observed within the spatial extent of this study. Instead, these results suggest that, in microtidal systems under high-discharge conditions, the near-field plume (Jirka et al., 1981) may extend for several kilometres onto the shelf, with the dynamical transition to subcritical flow occurring further offshore.

https://doi.org/10.5194/egusphere-2026-1840
Preprint. Discussion started: 23 April 2026

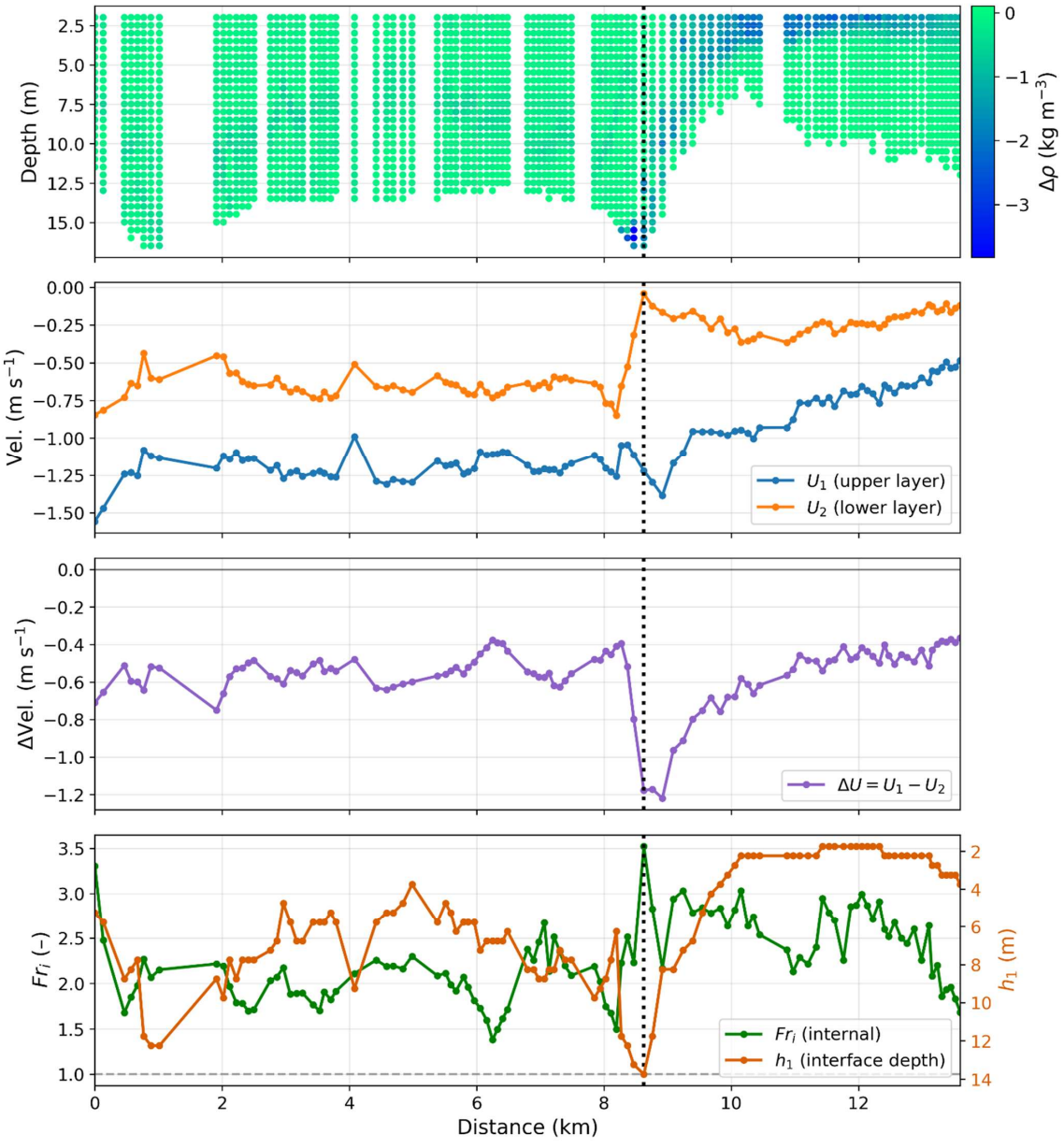

650 **Figure 13.** Two-layer parameters and Internal Froude Number as a function of distance. The figure consists of four vertical panels: **(a)** Vertical density gradient ($\Delta\rho$, kg m^{-3}) across depth; **(b)** Layer velocities, displaying the horizontal velocity (U, m s^{-1}) for upper (U_1) and

https://doi.org/10.5194/egusphere-2026-1840
Preprint. Discussion started: 23 April 2026

lower (U_2) layers; **(c)** Layer velocity difference (ΔU, m s^{-1}); and **(d)** Pycnocline depth (h_1, m, right axis) and the Internal Froude Number (Fr_i, left axis). The dashed horizontal line in panel (d) indicates the critical threshold (Fr_i = 1). The vertical dotted line marks the point of maximum constriction at the estuary–shelf interface.

5.4. Spatial Comparison and Estuarine Context

To evaluate the magnitude of the mixing processes observed, the maximum and minimum values of the primary hydrodynamic parameters were compared across the transition (Table 1) and contextualized with other estuarine systems globally (Table 2). The high-energy nature of the plume is initially evidenced by a peak in stratification ($N^2 \sim 10^{-1}$ s^{-2}) and vertical shear ($S^2 \sim 10^{-0.5}$ s^{-2}) that concentrate in the outer portion of the channel, marking the region of intense interfacial interaction (Fig. 9a, b). These conditions promote elevated TKE dissipation (ϵ), with peaks on the order of 10^{-3} W kg^{-1} recorded immediately adjacent to the mouth (Fig. 8).

Table 1. Range of hydrodynamic and turbulent parameters observed inside the channel and on the adjacent shelf. Values represent the absolute minimum and maximum recorded during the drift survey.

	Drift (Channel)		Drift (Shelf)	
	MAX	MIN	MAX	MIN
Salinity (g kg^{-1})	12.6	6.6	27.9	7.1
Temperature (^{0}C)	13	12.7	13.3	12.7
Density (kg m^{-3})	1009.1	1004.5	1020.8	1004.9
Along-channel Velocity (m s^{-1})	1.7	0.5	2.0	0.4
N^2 (s^{-2})	10^{-2}	10^{-3}	10^{-1}	10^{-5}
S^2(s^{-2})	10^{-1}	10^{-4}	$10^{-0.5}$	10^{-5}
ϵ (W kg^{-1})	10^{-4}	10^{-6}	10^{-3}	$10^{-7.5}$
A_z (m^2 s^{-1})	10^{-2}	10^{-5}	10^{-1}	10^{-7}

As synthesized in Table 2, the maximum dissipation rates recorded at the Patos Lagoon mouth and its adjacent plume place this microtidal system among the most energetic estuarine environments documented in the literature. The alignment of this highly energetic inlet with world-class systems such as the Gironde and Columbia estuaries (Table 2) confirms that intense

https://doi.org/10.5194/egusphere-2026-1840
Preprint. Discussion started: 23 April 2026

topographic constrictions can emulate the turbulent energy of macrotidal environments, even in the absence of a significant tidal range. Indeed, the dissipation observed is an order of magnitude higher than values reported for other microtidal river plumes, such as Connecticut (O'Donnell et al., 2008), and Magdalena (Álvarez-Silva et al., 2026) rivers. Furthermore, the extreme inertial dominance observed during this survey leads to dissipation rates that match or exceed those recorded in larger meso- and macrotidal systems, such as Gironde (Ross et al. 2019), Merrimack (MacDonald et al., 2007), Changjiang (Wang et al., 2020), Fraser (MacDonald and Geyer, 2004), and Hudson (Peters and Bokhorst, 2000) rivers. This energy level also significantly surpasses other topographically constrained environments in the Southern Hemisphere, including the Patagonian fjords, where tidal-driven turbulence at sills typically reaches values two orders of magnitude lower than those observed in the present study (Pérez-Santos et al., 2018).

Table 2. Global comparison of maximum TKE dissipation rates (ϵ) and tidal regimes across different estuarine systems.

System	Max. ϵ (W kg^{-1})	Tidal Regime	Reference
Patos Lagoon (Brazil)	10^{-3}	Microtidal	This study
Patos Lagoon (Brazil)	10^{-4}	Microtidal	Barros et al., (2025)
Columbia river (USA)	10^{-3} *	Mesotidal	Spicer (2022)
Gironde estuary (France)	10^{-3}	Macrotidal	Ross et al. (2019)
Merrimack river (USA)	10^{-3}	Mesotidal	MacDonald et al. (2007)
Changjiang (Yangtze river -China)	10^{-3}	Mesotidal	Wang et al. (2020)
Fraser river (Canada)	10^{-4}	Mesotidal	MacDonald and Geyer (2004)
Hudson river (USA)	10^{-4}	Mesotidal	Peters and Bokhorst (2000)
Connecticut river (USA)	10^{-4}	Microtidal	O'Donnell et al. (2008)
Magdalena river (Colombia)	10^{-4}	Microtidal	Álvarez-Silva et al. (2026)
Patagonian fjords (Chile)	10^{-5}	Mesotidal	Pérez-Santos et al. (2018)

*Transient peaks reaching 10^{-2} W kg^{-1} have been recorded during extreme tidal-front interactions (Spicer, 2022).

Consistent with these high dissipation rates, the vertical eddy viscosity (A_z) reached maximum values of approximately 10^{-1} m^2 s^{-1} within the plume's interface (Table 1). This magnitude surpasses the maximum value of 10^{-2} m^2 s^{-1} previously observed in the Patos Lagoon inlet (Barros et al., 2025), reinforcing that under high outflow and specific morphological constraints, the Patos Lagoon inlet functions as a high-energy 'nozzle' that maximizes turbulent transport to the inner shelf.

https://doi.org/10.5194/egusphere-2026-1840
Preprint. Discussion started: 23 April 2026

5.5 Turbulence and Mixing Processes

The buoyancy Reynolds number (Re_b) was applied to map the various stages of turbulence along the transect section (Fig. 10b). Dominant values of $Re_b > 200$ (blue points) are observed throughout most of the water column, indicating that vigorous, fully developed, and isotropic turbulence prevails in the system. In these regions, buoyancy forces are unable to inhibit the vertical transport of mass and momentum, a state that coincides with the high internal Froude number (Fr_i) values recorded (Fig. 13). This competition between shear and buoyancy was previously identified as a key driver of turbulence within the Patos Lagoon inlet (Barros et al., 2025), where Re_b often serves as a more sensitive indicator of mixing states than traditional stability metrics, as it directly scales the turbulence levels relative to the buoyancy-controlled Ozmidov scale (Stacey et al., 2012).

However, turbulence is locally suppressed within thin layers directly associated with the pycnocline interface (dashed line in Fig. 10b). In these specific pockets, particularly between km 4 and 8, $Re_b < 15$ occurs (red points), indicating a regime where stratification inhibits turbulent fluctuations and vertical mixing is restricted toward molecular levels (Shih et al., 2005). Surrounding these suppressed zones, a transitional regime ($15 < Re_b < 200$, yellow points) marks the areas where turbulence is active yet anisotropic. In this zone, mixing efficiency is typically maximized, suggesting that despite the reported sharp stratification, the interfacial shear at the plume front is the primary driver for pycnocline erosion and subsequent saltwater entrainment. Such behaviour demonstrates that the presence of stratification does not necessarily imply the complete suppression of turbulent mixing, even under established stratification (Huguenard et al., 2015).

This spatial distribution suggests that while the plume's massive inertia maintains a state of generalized high-energy mixing, the density interface still acts as a localized, albeit intermittent, barrier to vertical transport. In this context, metrics based on the Richardson number (R_i) provide a consistent view of the potential for stratification-driven stability, particularly near the mouth and along the offshore interface, where it indicates a robust buoyancy barrier (Fig. 9c).

However, the presence of these stable R_i layers does not necessarily imply the absence of mixing in such high-energy systems. While $R_i \approx 0.25$ is commonly interpreted as a classical threshold for the onset of shear instability, this criterion is not sufficient to fully describe mixing in natural environments, as turbulence may be sustained for R_i values approaching unity under energetic forcing conditions (Simpson and Sharples, 2012). As observed between km 9 and 10, even where R_i suggests stability, the buoyancy Reynolds number (Re_b) and elevated ϵ confirm that turbulence remains vigorous enough to dynamically erode the interface. In estuarine environments, this corresponds to an intermediate regime ($0.25 < R_i < 1$), where mixing is not suppressed but instead modulated by the interplay of shear, straining, and advection (Giddings et al., 2011).

https://doi.org/10.5194/egusphere-2026-1840
Preprint. Discussion started: 23 April 2026

These results suggest that the classical R_i threshold alone may not fully capture the complexity of mixing dynamics in this system. Such limitations of the gradient Richardson number as a universal mixing proxy have been recently documented in other diverse high-energy, wind-dominated systems (Arevalo et al., 2022; Álvarez-Silva et al., 2026), where vigorous mixing and asymmetric hydrodynamic structures persist even under seemingly stabilizing density gradients. Therefore, the buoyancy Reynolds number (Re_b) provides a more robust description of turbulent efficiency in this energetically active plume, capturing the full spectrum of mixing states that traditional stability thresholds may overlook.

6 Conclusions

This study provides a detailed characterization of the estuary-shelf transition of a buoyant plume during a period of high discharge, revealing how inlet morphology and inertial dominance redefine mixing processes. The Patos Lagoon inlet, despite its microtidal regime, represents a high-energy benchmark for global estuary-shelf transitions, where the terminal jetty constriction acts as a morphological "nozzle" that forces the flow into an extremely energetic state. These high dissipation levels, reaching 10^{-3} W kg^{-1} near the mouth, are comparable to those found in major meso- and macrotidal systems and are driven by surface velocities of ~ 2 m s^{-1}, where inertial momentum far outweighs the stabilizing effects of buoyancy.

The along-channel evolution of turbulent kinetic energy (TKE) dissipation exhibits morphological control. Dissipation rates (ϵ) are significantly reduced within the inner estuary where the cross-sectional area widens, while maximum values occur near the jetty-confined mouth. Following this peak, ϵ values decrease progressively as the flow spreads offshore and the plume expands laterally. This spatial evolution of turbulence is consistent with the dominant hydrodynamic regime, which remains supercritical ($Fr_i > 1$) throughout the sampled area. This high-momentum state effectively blocks the upstream propagation of internal disturbances. The observed downward trend of Fr_i offshore and the subsequent deepening of the pycnocline, suggests that the hydraulic adjustment toward subcritical conditions is displaced several kilometres onto the inner shelf.

Within this high-energy, supercritical regime, the interplay between buoyancy suppression and shear production is more effectively captured by the buoyancy Reynolds number (Re_b). This parameter accurately identifies the turbulence suppression observed near km 6, consistent with the localized minima in TKE dissipation. Furthermore, at the plume's frontal interface (~ km 9), Re_b provides a clearer explanation of the mixing state than the Richardson number; while R_i identifies the structural potential for stability along the interface, Re_b reveals a state of vigorous, fully developed turbulence ($Re_b > 200$). This contrast highlights the limitation of relying solely on stability-based metrics to describe mixing in such energetic environments.

The findings of this study underscore the dominant role of inlet morphology in modulating the hydrodynamic and mixing regimes of river plumes, suggesting that similar dynamics may occur in other high-discharge, wind-dominated estuaries, particularly in microtidal systems. While these results provide a detailed characterization of the source and buoyancy-forced

https://doi.org/10.5194/egusphere-2026-1840
Preprint. Discussion started: 23 April 2026

plume regions, explicitly closing the momentum budget remains a challenge for future research. In this context, targeted fieldwork focusing on hydraulic adjustments in the mid- to far-field plume will be essential to further elucidate mixing pathways in these active transition zones

Code and data availability

The hydrographic and microstructure data used in this study are available from the corresponding author upon reasonable request. The pre-processing Python routines are available at https://gutoschettini.github.io/Ocean-Data-Analysis-Python/ and archived in Zenodo (Schettini, 2021; https://doi.org/10.5281/zenodo.15442937), and the dedicated codebase developed for the turbulence analysis and stability metrics is archived in Zenodo (Barros, 2026; https://doi.org/10.5281/zenodo.18974391).

Supplement link

Empty.

Team list

Empty.

Author contributions

D. Barros: Methodology, Software, Formal analysis, Investigation, Visualization, Writing – original draft; L. Ross: Methodology, Software, Formal analysis, Supervision, Writing – review & editing; C. A. F. Schettini: Conceptualization, Methodology, Software, Formal analysis, Supervision, Funding acquisition, Writing – review & editing.

Competing interests

The authors declare that they have no known competing financial interests or personal relationships that could have appeared to influence the work reported in this paper.

Disclaimer

Copernicus Publications adds a standard disclaimer: “Copernicus Publications remains neutral with regard to jurisdictional claims made in the text, published maps, institutional affiliations, or any other geographical representation in this paper. While

https://doi.org/10.5194/egusphere-2026-1840
Preprint. Discussion started: 23 April 2026

Copernicus Publications makes every effort to include appropriate place names, the final responsibility lies with the authors. Views expressed in the text are those of the authors and do not necessarily reflect the views of the publisher."

Acknowledgements

We would like to thank all the individuals who aided during the fieldwork. We thank the Rio Grande Pilots for providing environmental data and support during the fieldwork. Lauren Ross would like to acknowledge funding from the National Science Foundation Grant No. 2045866. This work was supported by the Brazilian National Research Council CNPq under Grant No. 443490/2023-6. Carlos A.F. Schettini research fellowship CNPq 309572/2025-8.

Financial support

Empty.

Review statement

Empty.

References

ALM – Agência da Lagoa Mirim: Bacia da Lagoa Mirim, available at: https://wp.ufpel.edu.br/alm, last access: 10 September 2023.

Álvarez-Silva, O., Becker, M., Flores, R. P., Arévalo, F., Holtermann, P., Cardona, Y., and Winter, C.: The asymmetric hydrodynamic structure of a wind-dominated river plume, J. Geophys. Res.-Oceans, 131, e2025JC022720, https://doi.org/10.1029/2025JC022720, 2026.

ANA – Agência Nacional de Águas e Saneamento Básico: Hidroweb database, available at: https://www.snirh.gov.br/hidroweb, last access: 10 September 2023.

Arevalo, F. M., Álvarez-Silva, O., Caceres-Euse, A., and Cardona, Y.: Mixing mechanisms at the strongly-stratified Magdalena River's estuary and plume, Estuar. Coast. Shelf S., 277, 108077, https://doi.org/10.1016/j.ecss.2022.108077, 2022.

Ávila, R. A. and Calil, P. H. R.: Buoyancy-driven effects on turbulent diffusivity induced by a river plume in the southern Brazilian shelf, Ocean Sci. Discuss., 1–32, https://doi.org/10.5194/os-2018-66, 2018.

Barros, D.: Codebase for Barros et al., 2026 (v1.0.0), Zenodo [code], https://zenodo.org/records/18974391, 2026.

Barros, D., Bayley, T., Ross, L., and Schettini, C. A. F.: Spatial variability of turbulent mixing in a highly stratified system, J. Marine Syst., 250, 104071, https://doi.org/10.1016/j.jmarsys.2025.104071, 2025.

https://doi.org/10.5194/egusphere-2026-1840
Preprint. Discussion started: 23 April 2026

Burrage, D., Wesson, J., Martinez, C., Pérez, T., Möller Jr., O. O., and Piola, A.: Patos Lagoon Outflow within the Rio de la Plata Plume Using an Airborne Salinity Mapper: Observing an Embedded Plume, Cont. Shelf Res., 28, 1625–1638, https://doi.org/10.1016/j.csr.2007.02.014, 2008.

Cai, W.-J., Chen, C. T. A., and Borges, A.: Carbon dioxide dynamics and fluxes in coastal waters influenced by river plumes, in: Biogeochemical Dynamics at Major River-Coastal Interfaces, edited by: Bianchi, T. S., Allison, M. A., and Cai, W.-J., Cambridge University Press, Cambridge, 155–173, https://doi.org/10.1017/CBO9781139136853.010, 2013.

Campos, E. J. D., Piola, A. R., Matano, R. P., and Miller, J. L.: PLATA: A synoptic characterization of the southwest Atlantic shelf under influence of the Plata River and Patos Lagoon outflows, Cont. Shelf Res., 28, 1551–1555, https://doi.org/10.1016/j.csr.2008.03.007, 2008.

Chao, S.-Y. and Boicourt, W. C.: Onset of estuarine plumes, J. Phys. Oceanogr., 16, 2137–2149, 1986.

Cole, K. L., MacDonald, D. G., Kakoulaki, G., and Hetland, R. D.: River plume source-front connectivity, Ocean Model., 150, 101571, https://doi.org/10.1016/j.ocemod.2020.101571, 2020.

Cruz, G. O. and Schettini, C. A. F.: The dynamics of the inner-shelf suspended sediments based on ADCP records and Rouse theory, Cont. Shelf Res., 289, 105467, https://doi.org/10.1016/j.csr.2025.105467, 2025.

Delatolas, N., MacDonald, D. G., Goodman, L., Whitney, M., Huguenard, K., and Cole, K.: Comparison of structure and turbulent mixing between lateral and leading-edge river plume fronts: Microstructure observations from a T-REMUS AUV, Estuar. Coast. Shelf S., 283, 108234, https://doi.org/10.1016/j.ecss.2023.108234, 2023.

Dorrell, R. M., Peakall, J., Sumner, E. J., Parsons, D. R., Darby, S. E., Wynn, R. B., Özsoy, E., and Tezcan, D.: Flow dynamics and mixing processes in hydraulic jump arrays: Implications for channel-lobe transition zones, Mar. Geol., 381, 181–193, https://doi.org/10.1016/j.margeo.2016.09.009, 2016.

Dyer, K. R.: Estuarine hydrography and sedimentation: a handbook, Cambridge University Press, Cambridge, UK, 239 pp., 1979.

Fennel, W. and Mutzke, A.: The initial evolution of a buoyant plume, J. Marine Syst., 12, 53–68, https://doi.org/10.1016/S0924-7963(96)00088-7, 1997.

Fernandes, E. H. L., Dyer, K. R., and Möller, O. O.: Spatial Gradients in the Flow of Southern Patos Lagoon, J. Coastal Res., 21, 4, 759–769, https://doi.org/10.2112/006-NIS.1, 2005.

Gargett, A. E., Osborn, T. R., and Nasmyth, P. W.: Local isotropy and the decay of turbulence in a stratified fluid, J. Fluid Mech., 144, 231–280, https://doi.org/10.1017/S0022112084001592, 1984.

Geyer, W. R., Lavery, A. C., Scully, M. E., and Trowbridge, J. H.: Mixing by shear instability at high Reynolds number, Geophys. Res. Lett., 37, L22607, https://doi.org/10.1029/2010GL045272, 2010.

Geyer, W. R., Ralston, D. K., and Holleman, R. C.: Hydraulics and mixing in a laterally divergent channel of a highly stratified estuary, J. Geophys. Res.-Oceans, 122, 4743–4760, https://doi.org/10.1002/2016JC012455, 2017.

https://doi.org/10.5194/egusphere-2026-1840
Preprint. Discussion started: 23 April 2026

Giddings, S. N., Fong, D. A., and Monismith, S. G.: Role of straining and advection in the intratidal evolution of stratification, vertical mixing, and longitudinal dispersion of a shallow, macrotidal, salt wedge estuary, J. Geophys. Res.-Oceans, 116, C03003, https://doi.org/10.1029/2010JC006482, 2011.

Goodman, L., Levine, E. R., and Lueck, R. G.: On measuring the terms of the turbulent kinetic energy budget from an AUV, J. Atmos. Ocean. Tech., 23, 977–999, https://doi.org/10.1175/JTECH1889.1, 2006.

Gregg, M. C., D'Asaro, E. A., Riley, J. J., and Kunze, E.: Mixing efficiency in the ocean, Annu. Rev. Mar. Sci., 10, 443–473, https://doi.org/10.1146/annurev-marine-121916-063643, 2018.

Hartmann, C. and Schettini, C. A. F.: Aspectos Hidrológicos Na Desembocadura Da Laguna Dos Patos, RS, Rev. Bras. Geociênc., 21, 371–377, https://doi.org/10.25249/0375-7536.1991371377, 1991.

Hetland, R. D.: Relating river plume structure to vertical mixing, J. Phys. Oceanogr., 35, 1667–1688, https://doi.org/10.1175/JPO2774.1, 2005.

Hetland, R. D.: The effects of mixing and spreading on density in near-field river plumes, Dynam. Atmos. Oceans, 49, 37–53, https://doi.org/10.1016/j.dynatmoce.2008.11.003, 2010.

Holleman, R. C., Geyer, W. R., and Ralston, D. K.: Stratified turbulence and mixing efficiency in a salt wedge estuary, J. Phys. Oceanogr., 46, 1769–1783, https://doi.org/10.1175/JPO-D-15-0193.1, 2016.

Horner-Devine, A. R., Hetland, R. D., and MacDonald, D. G.: Mixing and transport in coastal river plumes, Annu. Rev. Fluid Mech., 47, 569–594, https://doi.org/10.1146/annurev-fluid-010313-141408, 2015.

Huguenard, K. D., Valle-Levinson, A., Li, M., Chant, R. J., and Souza, A. J.: Linkage between lateral circulation and near-surface vertical mixing in a coastal plain estuary, J. Geophys. Res.-Oceans, 120, 4048–4067, https://doi.org/10.1002/2014JC010679, 2015.

Ivey, G. N., Winters, K. B., and Koseff, J. R.: Density stratification, turbulence, but how much mixing?, Annu. Rev. Fluid Mech., 40, 169–184, https://doi.org/10.1146/annurev.fluid.39.050905.110314, 2008.

Jirka, G. H., Stolzenbach, K. D., and Adams, E. E.: Buoyant Surface Jets, J. Hydraul. Eng., 107, 1467–1487, 1981.

Kay, D. J. and Jay, D. A.: Interfacial mixing in a highly stratified estuary: 1. Characteristics of mixing, J. Geophys. Res., 108, 3072, https://doi.org/10.1029/2000JC000252, 2003.

Kirinus, E. P., Marques, W. C., Costa, J., and Fernandes, E. H. L.: The Contribution of Waves in Mixing Processes of the Patos Lagoon Plume, Int. J. Geosci., 3, 1019–1026, https://doi.org/10.4236/ijg.2012.35102, 2012.

Kjerfve, B.: Manual for investigation of hydrological processes in mangrove ecosystems, University of South Carolina, Baruch Institute for Marine Biology and Coastal Research, Columbia, 79 pp., 1990.

Kjerfve, B. and Magill, K. E.: Comparative oceanography of coastal lagoons, in: Estuarine Variability, edited by: Wolfe, D. A., Academic Press, 63–81, https://doi.org/10.1016/B978-0-12-761890-6.50009-5, 1989.

Lohrenz, S. E., Cai, W.-J., Chakraborty, S., Gundersen, K., and Murrell, M. C.: Nutrient and carbon dynamics in a large river-dominated coastal ecosystem: the Mississippi-Atchafalaya River system, in: Biogeochemical Dynamics at Major River-Coastal Interfaces, Cambridge University Press, 448–472, https://doi.org/10.1017/CBO9781139136853.023, 2013.

https://doi.org/10.5194/egusphere-2026-1840
Preprint. Discussion started: 23 April 2026

Lueck, R.: Calculating the Rate of Dissipation of Turbulent Kinetic Energy, Rockland Scientific Technical Note 028, Victoria, BC, Canada, 2013.

Lueck, R., Wolk, F., and Black, K.: Measuring tidal channel turbulence with a Vertical Microstructure Profiler (VMP), Rockland Scientific Technical Note 026, Victoria, BC, Canada, 2013.

Lueck, R., Murowinski, E., and McMillan, J.: A Guide to Data Processing, Rockland Scientific Technical Note 039, Victoria, BC, Canada, 2020.

MacDonald, D. G. and Geyer, W. R.: Turbulent energy production and entrainment at a highly stratified estuarine front, J. Geophys. Res., 109, C05004, https://doi.org/10.1029/2003JC002094, 2004.

MacDonald, D. G., Goodman, L., and Hetland, R. D.: Turbulent dissipation in a near-field river plume: A comparison of control volume and microstructure observations with a numerical model, J. Geophys. Res.-Oceans, 112, C05026, https://doi.org/10.1029/2006JC004075, 2007.

Marques, W. C., Fernandes, E. H. L., Monteiro, I. O., and Möller, O. O.: Numerical modeling of the Patos Lagoon coastal plume, Brazil, Cont. Shelf Res., 29, 556–571, https://doi.org/10.1016/j.csr.2008.09.022, 2009.

Marques, W. C., Fernandes, E. H. L., Moraes, B. C., Möller, O. O., and Malcherek, A.: Dynamics of the Patos Lagoon coastal plume and its contribution to the deposition pattern of the southern Brazilian inner shelf, J. Geophys. Res., 115, C10045, https://doi.org/10.1029/2010JC006190, 2010.

Marques, W. C., Stringari, C. E., and Eidt, R. T.: The exchange processes of the Patos Lagoon estuary – Brazil: a typical El Niño year versus a normal meteorological conditions year, Adv. Water Resour. Prot., 2, 11–20, 2014.

McPherson, R. A., Stevens, C. L., and O'Callaghan, J.: Turbulent scales observed in a river plume entering a fjord, J. Geophys. Res.-Oceans, 124, 9190–9208, https://doi.org/10.1029/2019JC015448, 2019.

McPherson, R. A., Stevens, C. L., O'Callaghan, J. M., Lucas, A. J., and Nash, J. D.: The role of turbulence and internal waves in the structure and evolution of a near-field river plume, Ocean Sci., 16, 799–815, https://doi.org/10.5194/os-16-799-2020, 2020.

Miles, J. W.: On the stability of heterogeneous shear flows, J. Fluid Mech., 10, 496–508, https://doi.org/10.1017/S0022112061000305, 1961.

Miranda, L. B., Castro, B. M., and Kjerfve, B.: Princípios de Oceanografia Física de Estuários, Editora da Universidade de São Paulo, São Paulo, 2002.

Miranda, L. P., Machado, J. P., Saraiva, J. B., Barros, D. G., Goulart, E. S., and Andrade, H. N.: Meteoceanographic patterns associated with severe coastal storms along the southern coast of Brazil, Meteorology, 5, 1, https://doi.org/10.3390/meteorology5010001, 2026.

Möller, O. O. and Castaing, P.: Hydrographical Characteristics of the Estuarine Area of Patos Lagoon (30°S, Brazil), in: Estuaries of South America, edited by: Perillo, G. M. E., Pino Quivira, M. C., Piccolo, M. C., and Pino-Quivira, M., Springer, Berlin, Heidelberg, 83–100, https://doi.org/10.1007/978-3-642-60131-6_5, 1999.

https://doi.org/10.5194/egusphere-2026-1840
Preprint. Discussion started: 23 April 2026

Möller, O. O., Lorenzzentti, J. A., Stech, J. L., and Mata, M. M.: The Patos Lagoon summertime circulation and dynamics, Cont. Shelf Res., 16, 335–351, https://doi.org/10.1016/0278-4343(95)00014-R, 1996.

Möller, O. O., Castaing, P., Salomon, J. C., and Lazure, P.: The Influence of Local and Non-local Forcing Effects on the Subtidal Circulation of Patos Lagoon, Estuaries, 24, 297–311, https://doi.org/10.2307/1352953, 2001.

Möller, O. O., Castaing, P., Fernandes, E. H. L., and Lazure, P.: Tidal frequency dynamics of a Southern Brazil coastal lagoon: Choking and short period forced oscillations, Estuar. Coast., 30, 311–320, https://doi.org/10.1007/BF02700173, 2007.

Monismith, S. G.: Mixing in Estuaries, in: Contemporary Issues in Estuarine Physics, edited by: Valle-Levinson, A., Cambridge University Press, Cambridge, 145–185, https://doi.org/10.1017/CBO9780511676567.008, 2010.

Monteiro, I. O., Marques, W. C., Fernandes, E. H. L., Gonçalves, R. C., and Möller Jr., O. O.: On the effect of Earth rotation, river discharge, tidal oscillations, and wind in the dynamics of the Patos Lagoon coastal plume, J. Coastal Res., 27, 120–130, 2011.

Nash, J. D. and Moum, J. N.: River plumes as a source of internal gravity waves in the coastal ocean, Nature, 437, 400–403, https://doi.org/10.1038/nature03936, 2005.

Nash, J. D., Kilcher, L. F., and Moum, J. N.: Structure and composition of a strongly stratified, tidally pulsed river plume, J. Geophys. Res., 114, C00B12, https://doi.org/10.1029/2008JC005036, 2009.

O'Donnell, J., Ackleson, S. G., and Levine, E. R.: On the spatial scales of a river plume, J. Geophys. Res., 113, C04017, https://doi.org/10.1029/2007JC004440, 2008.

Pérez-Santos, I., Castro, L., Ross, L., Niklitschek, E., Mayorga, N., Cubillos, L., Gutierrez, M., Escalona, E., Castillo, M., Alegría, N., and Daneri, G.: Turbulence and hypoxia contribute to dense biological scattering layers in a Patagonian fjord system, Ocean Sci., 14, 1185–1206, https://doi.org/10.5194/os-14-1185-2018, 2018.

Peters, H. and Bokhorst, R.: Microstructure observations of turbulent mixing in a partially mixed estuary. Part I: Dissipation rate, J. Phys. Oceanogr., 30, 1232–1244, https://doi.org/10.1175/1520-0485(2000)030<1232:MOOTMI>2.0.CO;2, 2000.

Piola, A. R., Matano, R. P., Palma, E. D., Möller Jr., O. O., and Campos, E. J. D.: The influence of the Plata River discharge on the western South Atlantic shelf, J. Geophys. Res.-Oceans, 110, C12038, https://doi.org/10.1029/2004GL021638, 2005.

Ross, L., Huguenard, K. D., and Sottolichio, A.: Intratidal and fortnightly variability of vertical mixing in a macrotidal estuary: The Gironde, J. Geophys. Res.-Oceans, 124, 2641–2659, https://doi.org/10.1029/2018JC014456, 2019.

Santa-Rosa, P. R. A. and Schettini, C. A. F.: Daily variability of estuary-shelf exchange at the Lagoa dos Patos's mouth, Reg. Stud. Mar. Sci., 77, 103633, https://doi.org/10.1016/j.rsma.2024.103633, 2024.

Schettini, C. A. F.: Ocean Data Analysis with Python/Jupyter (v1.0), Zenodo [code], https://doi.org/10.5281/zenodo.15442937, 2021.

Schettini, C. A. F., Kuroshima, K. N., Pereira Filho, J., Rörig, L. R., and Resgalla Jr., C.: Oceanographic and ecological aspects of the Itajaí-Açu River plume during a high discharge period, An. Acad. Bras. Cienc., 70, 335–351, 1998.

https://doi.org/10.5194/egusphere-2026-1840
Preprint. Discussion started: 23 April 2026

Shih, L. H., Koseff, J. R., Ivey, G. N., and Ferziger, J. H.: Parametrization of turbulent fluxes and scales using homogeneous sheared stably stratified turbulence simulations, J. Fluid Mech., 525, 193–214, https://doi.org/10.1017/S0022112004002587, 2005.

Simão, R., Tavora, J., Salama, S., Weschenfelder, J., Molano Cárdenas, S. M., Gonçalves, G. M. S., Collares, G. L., Cavalcanti, A., Mendes, C. R. B., Barros, D., Pereira, E., Galetti, J., Möller, O., Jamet, C., and Fernandes, E. H.: Unprecedented suspended solids load caused by record-breaking extremes in southern Brazil: The May 2024 event, Front. Mar. Sci., 12, 1726787, https://doi.org/10.3389/fmars.2025.1726787, 2026.

Simpson, J. H., and Sharples, J.: Introduction to the Physical and Biological Oceanography of Shelf Seas, Cambridge University Press, Cambridge, 424 pp., 2012.

Sims, R. P., Bedington, M., Schuster, U., Watson, A. J., Kitidis, V., Torres, R., Findlay, H. S., Fishwick, J. R., Brown, I., and Bell, T. G.: Tidal mixing of estuarine and coastal waters in the western English Channel is a control on spatial and temporal variability in seawater CO_2, Biogeosciences, 19, 1657–1674, https://doi.org/10.5194/bg-19-1657-2022, 2022.

Soares, I. D., Kourafalou, V., and Lee, T. N.: Circulation on the western South Atlantic continental shelf: 2. Spring and autumn realistic simulations, J. Geophys. Res., 112, C04003, https://doi.org/10.1029/2006JC003620, 2007.

Spicer, P.: Mixing Processes in Tidally Pulsed River Plumes: Mechanisms, Significance, and Variability, PhD thesis, University of Maine, Orono, USA, [online] Available from: https://digitalcommons.library.umaine.edu/etd/3612, 2022.

Stacey, M. T., Monismith, S. G., and Burau, J. R.: Observations of turbulence in a partially stratified estuary, J. Phys. Oceanogr., 29, 1950–1970, https://doi.org/10.1175/1520-0485(1999)029<1950:OOTIAP>2.0.CO;2, 1999.

Stacey, M. T., Rippeth, T. P., and Nash, J. D.: Turbulence and Stratification in Estuaries and Coastal Seas, in: Treatise on Estuarine and Coastal Science, edited by: Wolanski, E. and McLusky, D., Elsevier, 121–148, https://doi.org/10.1016/B978-0-12-374711-2.00204-7, 2012.

Stips, A.: Dissipation Measurement: Theory, in: Marine Turbulence: Theories, Observations and Models, edited by: Baumert, H. Z., Simpson, J. H., and Sündermann, J., Cambridge University Press, Cambridge, 2005.

Thomson, R. E. and Emery, W. J.: Data analysis methods in physical oceanography, 3rd edn., Elsevier, Waltham, MA, 2014.

Thorpe, S. A.: An introduction to ocean turbulence, Cambridge University Press, Cambridge, 266 pp., 2007.

Thorpe, S. A., Malarkey, J., Voet, G., Alford, M. H., Girton, J. B., and Carter, G. S.: Application of a model of internal hydraulic jumps, J. Fluid Mech., 834, 125–148, https://doi.org/10.1017/jfm.2017.646, 2017.

Valle-Levinson, A., Klinck, J. M., and Wheless, G. H.: Inflows/outflows at the transition between a coastal plain estuary and the coastal ocean, Cont. Shelf Res., 16, 1819–1847, https://doi.org/10.1016/0278-4343(96)00016-7, 1996.

Vaz, A. C., Möller Jr., O. O., and Almeida, T. L.: Análise quantitativa da descarga dos rios afluentes da Lagoa dos Patos, Atlântica, 28, 13–24, https://doi.org/10.5088/atlantica.v28i1.1724, 2011.

Venayagamoorthy, S. K. and Koseff, J. R.: On the flux Richardson number in stably stratified turbulence, J. Fluid Mech., 798, R1, https://doi.org/10.1017/jfm.2016.340, 2016.

https://doi.org/10.5194/egusphere-2026-1840
Preprint. Discussion started: 23 April 2026

Wang, J., Yu, F., Ren, Q., Si, G., and Wei, C.: Spatial and temporal variability of turbulent mixing in the near field of the Changjiang River, J. Oceanol. Limnol., 38, 1138–1152, https://doi.org/10.1007/s00343-020-0008-7, 2020.

Wu, D., Chen, J., Wang, K., Ni, X., Li, D., Zeng, D., Fan, W., and Xu, D.: The Changjiang River plume shifts from carbon source to sink when net community production exceeds a threshold in early autumn, Sci. Total Environ., 888, 164126, https://doi.org/10.1016/j.scitotenv.2023.164126, 2023.

Zavialov, P. O., Pelevin, V. V., Belyaev, N. A., Izhitskiy, A. S., Konovalov, B. V., Krementskiy, V. V., Goncharenko, I. V., Osadchiev, A. A., Soloviev, D. M., Garcia, C. A. E., Pereira, E. S., Sartorato, L., and Möller, O. O.: High resolution LiDAR measurements reveal fine internal structure and variability of sediment-carrying coastal plume, Estuar. Coast. Shelf S., 205, 40–45, https://doi.org/10.1016/j.ecss.2018.01.008, 2018.